Journal of Computational Physics **170,** 39–80 (2001)
doi:10.1006/jcph.2001.6719, available online at http://www.idealibrary.com on IDEAL®

Convergent Cartesian Grid Methods for Maxwell's Equations in Complex Geometries

A. Ditkowski,* K. Dridi,† and J. S. Hesthaven*,[1]

*Division of Applied Mathematics, Brown University, Box F, Providence, Rhode Island 02912; †Optics and Fluid Dynamics Department, Risø National Laboratory, DK-4000 Roskilde, Denmark
E-mail: adit@cfm.brown.edu; kim.dridi@risoe.dk; Jan.Hesthaven@brown.edu

Received October 6, 1999; revised September 19, 2000

A convergent second-order Cartesian grid finite difference scheme for the solution of Maxwell's equations is presented. The scheme employs a staggered grid in space and represents the physical location of the material and metallic boundaries correctly, hence eliminating problems caused by staircasing, and, contrary to the popular Yee scheme, enforces the correct jump-conditions on the field components across material interfaces. A detailed analysis of the accuracy of the new embedding scheme is presented, confirming its second-order global accuracy. Furthermore, the scheme is proven to be a bounded error scheme and thus convergent. Conditions for fully discrete stability is furthermore established. This enables the derivation of bounds for fully discrete stability with CFL-restrictions being almost identical to those of the much simpler Yee scheme. The analysis exposes that the effects of staircasing as well as a lack of properly enforced jump-conditions on the field components have significant consequences for the global accuracy. It is, among other things, shown that for cases in which a field component is discontinuous along a grid line, as happens at general two- and three-dimensional material interfaces, the Yee scheme may exhibit local divergence and loss of global convergence. To validate the analysis several one- and two-dimensional test cases are presented, showing an improvement of typically 1 to 2 orders of accuracy at little or no additional computational cost over the Yee scheme, which in most cases exhibits first order accuracy.

Key Words: finite difference schemes; Maxwell's equations; complex geometries; embedded interfaces; stability; staircasing.

1. INTRODUCTION

The development of efficient, yet simple, computational methods for the accurate time-domain solution of Maxwell's equations remains a very significant challenge for several

[1] Corresponding author.

0021-9991/01 $35.00

reasons. The wave nature of the basic phenomena requires that one carefully considers even small local errors as they eventually may propagate to a different location and ruin the overall accuracy. Furthermore, the requirement that the scheme be able to propagate waves accurately and efficiently over many periods is a problem of central concern. This latter problem has received much attention in recent years through the attempt to apply high-order finite difference scheme, see [1] and references therein, and multidomain spectral methods [2–4]. These methods, however, share the disadvantage either that they are restricted to simple geometries or that a multidomain framework must be introduced to facilitate the correct treatment of general metallic boundaries and material interfaces, hence introducing a need for automated grid-generation, which remains a nontrivial task.

This situation is contrary to the very popular Yee scheme, introduced in [5], which utilizes an embedding technique by simply assigning appropriate material properties to the various grid points that form a simple Cartesian grid. The formally second-order accurate scheme employs a fully staggered space–time grid [6]. This straightforward approach remains by far the most popular time-domain computational technique for the modeling and design of problems in computational electromagnetics. An updated review and numerous examples of the usefulness of this simple approach can be found in [1, 7].

It is, however, well known that the straightforward embedding of an arbitrary volume in the grid introduces a number of more subtle problems. The inability of the simple embedding technique to account accurately for the position and shape of the boundaries of the embedded volumes requires one to approximate the boundaries and interfaces by a staircased curve. While this may seem adequate for many problems, it nevertheless affects the overall accuracy and essentially makes the scheme first order. In the case of metallic boundaries, this problem has received considerable interest in the past, see e.g. [8–10], and a number of resolutions have been suggested, e.g., local grid-refinements [11] and locally conforming FDTD methods [12, 13], contour path methods [14], and nonorthogonal curvilinear FDTD methods [15, 16], and time-domain finite volume methods on fully unstructured grids [17, 18]. A variety of other techniques can be found described in [1, 7]. Most, if not all, of these methods, however, sacrifice the simplicity of the original Yee scheme to achieve the improved accuracy.

A more subtle problem that has received significantly less attention is the effect of using staircasing around a nonmetallic embedded interface, i.e., a transparent interface. Although the conditions connecting the field components on both sides of such media are well known, no effort is made in the Yee scheme to enforce these conditions. To overcome the obvious problems associated with such an approach, the standard technique is to extend the size of the interface by introducing a transition zone in which averaged material properties are employed. While such techniques appear to improve the overall accuracy, it has nevertheless been shown that the global accuracy of the scheme is reduced to first order [19]. This is a one-dimensional result and, as we shall show here, the situation may be considerably worse for problems beyond one dimension.

The need to accurately model the location and the physical properties of embedded interfaces is not new nor is it restricted to the area of computational electromagnetics. Indeed, much work aimed at resolving such issues has appeared in the context of the modeling of seismic waves, acoustic lenses, and ultrasound imaging. The methods developed for such problems are often termed embedded interface methods (see, e.g., [20] and references therein) to reflect the basic idea that a simple Cartesian grid is maintained and the finite difference stencils around the embedded interfaces are modified to account for the correct

position of the interface and the proper physical jump-conditions. Many of these methods, however, involved the solution of the scalar wave-equation rather than the full system of equations as is the area of main interest when solving Maxwell's equations.

To address specifically the problems associated with the solution of Maxwell's equations using embedded metallic and general material interfaces, we present in this work a novel finite-difference scheme that maintains global second convergence in the presence of arbitrary interfaces, curved as well as straight. Moreover, and contrary to previous efforts, we prove convergence rigorously and show through detailed theoretical and computational comparisons with the Yee scheme the clear advantages of using this new scheme. Among the many results presented it is worth noting that staircasing problems at metallic boundaries are resolved at no additional computational cost, and internal material interfaces are treated in an equally efficient way. Indeed, the main additional computational cost of this new scheme lies in a preprocessing stage and adds only little to the cost of solving the time-dependent problem.

This paper is organized as follows. In Section 2 we discuss the details of the proposed scheme in a one-dimensional setting. Apart from providing the simplicity that allows one to appreciate the various elements of the scheme, the one-dimensional problem also lends itself to a complete analysis in terms of accuracy, stability, and convergence. The results of the analysis is supported by a number of examples that compare the performance of the new scheme with that of the traditional Yee scheme. Particular concerns related to the solution of Maxwell's equations beyond one dimension are discussed in Section 3 in which the basis solution techniques for general two- and three-dimensional situations are outlined. Issues related to efficient implementations are also addressed and a number of test cases illustrate the performance of the new scheme for two-dimensional problems and exposes many troubling problems with the Yee scheme. Section 4 contains a few concluding remarks and ideas for future work.

2. THE ONE-DIMENSIONAL SCHEME

To illustrate the central elements of the proposed scheme, let us consider the solution of the one-dimensional Maxwell equation

$$\begin{aligned} \varepsilon \frac{\partial E}{\partial t} &= \frac{\partial H}{\partial z}, \\ \mu \frac{\partial H}{\partial t} &= \frac{\partial E}{\partial z}, \end{aligned} \tag{1}$$

where $E(z,t)$ and $H(z,t)$ signifies the mutually perpendicular tangential electric and magnetic field components, while ε and μ refer to the relative permitivity and permeability, respectively, of the materials. The normalized quantities in Eq. (1) are related to the physical quantities, $\tilde{t}$, $\tilde{z}$, $\tilde{E}$, and $\tilde{H}$ as

$$t = \frac{c\tilde{t}}{L}, \quad z = \frac{\tilde{z}}{L}, \quad E = Z_0^{-1}\tilde{E}, \quad H = \tilde{H},$$

where $c = 1/\sqrt{\varepsilon_0\mu_0}$ is the vacuum speed of light with ε_0 and μ_0 being the vacuum permitivity and permeability, respectively, and $Z_0 = \sqrt{\mu_0/\varepsilon_0}$ is the vacuum impedance. The expression L is an appropriate length scale, usually taken as the mean wavelength, λ,

of the electromagnetic wave. In this setting, Eq. (1) describes waves propagating at unit speed and with lengths measured in units of wavelengths.

In case of a perfectly conducting wall (PEC), the boundary conditions become

$$E(z_{\text{pec}}, t) = 0 \quad \text{or} \quad \left.\frac{\partial H}{\partial z}\right|_{z_{\text{pec}}} = 0, \tag{2}$$

where z_{pec} signifies the position of the wall. In case the interface has finite conductivity the field components, $(E^{(1)}, H^{(1)})$ and $(E^{(2)}, H^{(2)})$, in the two regions are continuous across the material interface, situated at z_{mat}, as

$$E^{(1)}(z_{\text{mat}}, t) = E^{(2)}(z_{\text{mat}}, t), \quad H^{(1)}(z_{\text{mat}}, t) = H^{(2)}(z_{\text{mat}}, t). \tag{3}$$

We recall that the solution to Eq. (1), subject to the boundary conditions, consists of two counter propagating waves.

To solve Eq. (1) numerically, we introduce a spatially staggered grid with grid size h as

$$z_j = hj, \quad z_{j+\frac{1}{2}} = h\left(j + \frac{1}{2}\right), \tag{4}$$

and embed the full problem into this simple Cartesian grid. To account for the possibility of the physical problem not being aligned with the grid, we introduce $\gamma \in [0, \frac{1}{2}]$ which measures the relative distance between the physical boundary and the first grid point; see Fig. 1.

The two field components, E and H, are collocated as

$$E(z_j, t) = E_j(t), \quad H\left(z_{j+\frac{1}{2}}, t\right) = H_{j+\frac{1}{2}}(t),$$

as illustrated in Fig. 1. The actual limits on j depends on the individual computational problem, and it should be clear that the first and last grid points in the computational domain can be E- as well as H-nodes. We recall that ε and μ may depend on z, possibly in a discontinuous manner, and that the location of such material interfaces and the enclosing walls need not be aligned with the grid.

If one were to employ a Yee scheme [7], being nothing more than a centered second-order finite difference approximation, for the spatial approximation it becomes

$$\varepsilon_j \frac{dE_j}{dt} = \frac{H_{j+\frac{1}{2}} - H_{j-\frac{1}{2}}}{h}, \quad \mu_{j+\frac{1}{2}} \frac{dH_{j+\frac{1}{2}}}{dt} = \frac{E_{j+1} - E_j}{h}, \tag{5}$$

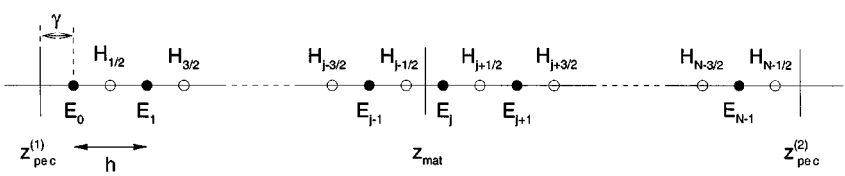

FIG. 1. Illustration of a general situation in which the computational problem is entirely embedded in a Cartesian staggered grid. The walls, situated at $z^{(1)}_{\text{pec}}$ and $z^{(2)}_{\text{pec}}$, are assumed to be perfect conductors while a material interface is positioned at z_{mat}.

with no special effort being made to properly account for the correct position of the material interfaces or the enclosing walls. Moreover, in regions where the material properties varies discontinuously, this approach implicitly assumes that the solution is at least twice differentiable—an assumption that clearly is violated, as one can only expect continuity across a material interface. As we shall see later, this latter problem is at least as significant as that of not properly accounting for the position of the walls and interfaces, known as the staircasing problem.

The use of a staggered grid has the advantage of reducing the local error with a factor of two without increasing the computational work and is a widely used technique for second-order schemes. However, as we shall see shortly, the staggering of the grid also has additional advantages when encountering interfaces that are not aligned with the grid.

2.1. Central Elements of the Scheme

To simplify the discussion and make the central ideas underlying the scheme appear as clear as possible, let us consider the situation of a perfectly conducting cavity, enclosed by two PEC walls situated at $z_{\text{pec}}^{(1)}$ and $z_{\text{pec}}^{(2)}$. The cavity is assumed to be filled with two regions of different materials, having properties $(\varepsilon^{(1)}, \mu^{(1)})$ and $(\varepsilon^{(2)}, \mu^{(2)})$, and with the interface situated at z_{mat}, as illustrated in Fig. 1. The generalization to multiple regions of different materials is straightforward.

For the sake of the discussion, let us introduce the two sets of fields, $(E^{(k)}, H^{(k)})$ with $k = 1, 2$, representing the solution in the two regions of different materials. We also assume that the two solutions are given on two separate grids and are connected only through the conditions across the material interface, Eq. (3), much as in a multielement solution technique. The general scenario is sketched in Fig. 2. For simplicity we assume here that N, being the number of grid points in each domain, is the same for each region. This, however, is done purely to simplify the notation and the generalization to a different number of grid points in each domain is straightforward.

To account for the situation where the interfaces, be they material interfaces or PEC walls, do not coincide with a grid point, we associate with each region two parameters, $\gamma_L^{(k)}$ and $\gamma_R^{(k)}$, as measures of the distance from the first/last grid point to the physical position of the wall or interface relative to the grid size h. Clearly, $\gamma^{(k)} \in [0, \frac{1}{2}]$ and, because of the global equidistant grid, $\gamma_R^{(k)} + \gamma_L^{(k+1)} = \frac{1}{2}$, across a material interface. Since these parameters are only geometry-dependent, they can be computed and stored in a preprocessing stage once the grid has been defined.

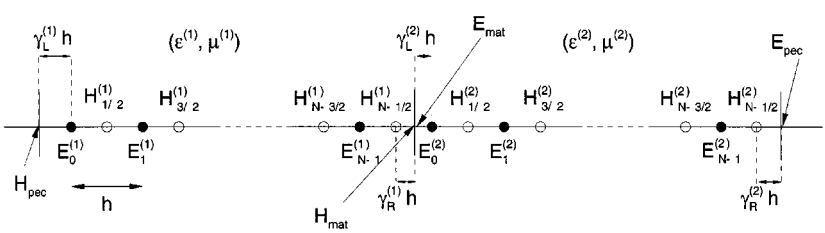

FIG. 2. Definition of grid, numbering and various parameters for solving the one-dimensional Maxwells equations in a PEC cavity filled with two materials.

In the interior of each of the two regions with smoothly varying material parameters, we shall use the standard staggered scheme

$$j \in [1, N-1]: \ \varepsilon^{(k)} \frac{dE_j^{(k)}}{dt} = \frac{H_{j+\frac{1}{2}}^{(k)} - H_{j-\frac{1}{2}}^{(k)}}{h}, \tag{6}$$

and

$$j \in [0, N-2]: \ \mu^{(k)} \frac{dH_{j+\frac{1}{2}}^{(k)}}{dt} = \frac{E_{j+1}^{(k)} - E_j^{(k)}}{h}, \tag{7}$$

where $k = 1, 2$ and the numbering follows that of Fig. 2. Without loss of generality we can assume that the material properties are constant within each region of the cavity. The subsequent discussion, however, extends trivially to include problems where the materials vary smoothly within each domain.

To complete the scheme we shall introduce special schemes for updating $E_0^{(k)}$ and $H_{N-\frac{1}{2}}^{(k)}$ in such a way that the boundary conditions at the PEC walls, the material interface, and the physical position of these relative to the grid is accounted for correctly.

Let us first focus the attention on the formulation of the scheme close to the perfectly conducting boundaries with the boundary conditions given in Eq. (2). Attempting to update $E_0^{(1)}$ we realize that this is complicated by the condition being of Neumann type, which we enforce through a second-order approximation, leading to a scheme for updating $E_0^{(1)}$ as

$$\varepsilon^{(1)} \frac{dE_0^{(1)}}{dt} = \frac{\gamma_L^{(1)}}{1 + \gamma_L^{(1)}} \frac{H_{\frac{3}{2}}^{(1)} - H_{\frac{1}{2}}^{(1)}}{h}. \tag{8}$$

The scheme for updating $H_{1/2}^{(1)}$ employs an asymmetric stencil,

$$\mu^{(1)} \frac{dH_{1/2}^{(1)}}{dt} = \frac{E_1^{(1)} - E_{\text{pec}}}{\left(1 + \gamma_L^{(1)}\right)h} = \frac{E_1^{(1)}}{\left(1 + \gamma_L^{(1)}\right)h}, \tag{9}$$

and simply utilizes the wall condition for computing the flux rather than $E_0^{(1)}$ directly. Note that $\gamma_L^{(1)} = 0$ recovers the simple staggered scheme, Eq. (7).

The scheme for updating $H_{N-\frac{1}{2}}^{(2)}$ is simpler, as we can explicitly exploit that $E^{(2)}(z_{\text{pec}}) = E_{\text{pec}} = 0$ to obtain

$$\mu^{(2)} \frac{dH_{N-\frac{1}{2}}^{(2)}}{dt} = \frac{2}{2\gamma_R^{(2)} + 1} \frac{E_{\text{pec}} - E_{N-1}^{(2)}}{h} = \frac{2}{2\gamma_R^{(2)} + 1} \frac{-E_{N-1}^{(2)}}{h}. \tag{10}$$

Let us now consider the treatment of the material interfaces across which we know that the individual field components must remain continuous. However, one cannot, as is implicitly done in the traditional Yee scheme, assume that the fields are smooth across the boundary and simply use $E_{N-1}^{(1)}$ and $E_0^{(2)}$ to update $H_{N-1/2}^{(1)}$.

To address this problem, we introduce the extrapolated value

$$E_{\text{mat}} = \left(1 + \gamma_L^{(2)}\right) E_0^{(2)} - \gamma_L^{(2)} E_1^{(2)}, \tag{11}$$

and complete the scheme for updating $H^{(1)}_{N-1/2}$ as

$$\mu^{(1)} \frac{dH^{(1)}_{N-1/2}}{dt} = \frac{2}{2\gamma^{(1)}_R + 1} \frac{E_{\text{mat}} - E^{(1)}_{N-1}}{h}. \tag{12}$$

Likewise we compute the flux of $E^{(2)}_0$ by using the extrapolated magnetic field

$$H_{\text{mat}} = \left(1 + \gamma^{(1)}_R\right) H^{(1)}_{N-1/2} - \gamma^{(1)}_R H^{(1)}_{N-3/2}, \tag{13}$$

to obtain

$$\varepsilon^{(2)} \frac{dE^{(2)}_0}{dt} = \frac{2}{2\gamma^{(2)}_L + 1} \frac{H^{(2)}_{1/2} - H_{\text{mat}}}{h}. \tag{14}$$

Before proceeding with a rigorous analysis of the scheme outlined in Eqs. (6)–(14), it is worthwhile making a few observations. A key property of the scheme can be appreciated by observing that $\gamma^{(k)}$ always appear as $\alpha\gamma^{(k)} + 1 (\alpha = 1$ at metals, otherwise $\alpha = 2)$ whenever appearing in the denominator. As a consequence, the scheme can be expected to be well behaved for all values of γ_R and γ_L. The reason for this property can be found in the use of the staggered grid, i.e., if a scheme using a regular grid was being generalized naively, the corresponding denominator would be proportional to $\gamma^{(k)}$ and one would expect severe stability problems for $\gamma^{(k)}$ approaching zero. These considerations are confirmed in Section 2.3, where we show that the maximum time-step is bounded from below for a fixed grid-size and all values of γ_L and γ_R.

One should also observe that we have chosen to describe the scheme in a method-of-lines framework and have not specified the scheme for advancing in time. A natural choice could be to also stagger in time, using the leapfrog scheme, although we shall use a Runge–Kutta scheme for the temporal integration. While the main reason for this is the potential of implementing a fully fourth-order scheme within the same framework, it also has the advantage of not suffering from the parasitic mode of the leapfrog scheme and of being self-starting. Moreover, from a practical point of view, it is often advantageous to have all field components at the same time levels for the purpose of postprocessing and data analysis.

2.2. Accuracy

While the staggered scheme in Eqs. (6) and (7), utilized in the interior of the regions, is well understood, the impact of the proposed modifications along interfaces on such critical properties as accuracy and stability is not at all obvious.

We shall begin this discussion by first analyzing the local accuracy of the scheme. Recall that the local truncation error, $\tau^{(k)}_j$ and $\tau^{(k)}_{j+\frac{1}{2}}$, for the E and H component, respectively, of the classic staggered scheme, Eqs. (6) and (7), used in the interior is

$$\tau^{(k)}_j = \frac{1}{24} h^2 \left.\frac{\partial^3 H}{\partial z^3}\right|_{z_j} + \mathcal{O}(h^4), \quad \tau^{(k)}_{j+\frac{1}{2}} = \frac{1}{24} h^2 \left.\frac{\partial^3 E}{\partial z^3}\right|_{z_{j+\frac{1}{2}}} + \mathcal{O}(h^4),$$

where we recognize the second-order behavior provided the exact solutions, E and H, are at least thrice differentiable. Following the analysis of [21], we can then allow the use of a local first-order scheme at a finite number of grid points and maintain global second-order convergence. This result shall be essential in the following.

Keep in mind that the temporal variable has not been discretized and no error from the time integration will be included in the subsequent analysis. For simplicity we shall not explicitly include reference to the time in the remaining analysis.

Let us now consider the effect of the variation of $\gamma^{(k)}$ on the accuracy of the scheme utilized at the perfectly conducting wall in Eqs. (8)–(10), and begin by analyzing the former, i.e., Eq. (8), from which we recover a local truncation error as

$$\tau_0^{(1)} = -\frac{1}{1+\gamma_L^{(1)}}\frac{\partial H^{(1)}}{\partial z}\bigg|_{z_0^{(1)}} + \frac{\gamma_L^{(1)}}{1+\gamma_L^{(1)}}h\frac{\partial^2 H^{(1)}}{\partial z^2}\bigg|_{z_0^{(1)}} + \mathcal{O}(h^2).$$

At first this appears as a rather unfortunate result, as a local nonconverging term is introduced. However, if we recall that at a PEC wall one has

$$\frac{\partial^{2p} E}{\partial z^{2p}} = 0, \quad \frac{\partial^{2p+1} H}{\partial z^{2p+1}} = 0, \tag{15}$$

as a direct consequence of the equations themselves, Eq. (1), and the boundary conditions, Eq. (2), one obtains, to first order in $\gamma^{(1)}h$, that

$$-\frac{1}{1+\gamma_L^{(1)}}\left[\frac{\partial H^{(1)}}{\partial z}\bigg|_{z_{\text{pec}}^{(1)}} + \gamma_L^{(1)}h\frac{\partial^2 H^{(1)}}{\partial z^2}\bigg|_{z_{\text{pec}}^{(1)}}\right] + \frac{\gamma_L^{(1)}}{1+\gamma_L^{(1)}}h\frac{\partial^2 H^{(1)}}{\partial z^2}\bigg|_{z_{\text{pec}}^{(1)}} = 0,$$

at the wall. Hence, the zeroth and the first-order term vanishes identically. Indeed, the leading local error term becomes

$$\tau_0^{(1)} = \frac{\gamma_L^{(1)}}{24\left(1+\gamma_L^{(1)}\right)}\left[8\left(\gamma_L^{(1)}\right)^2 + 13\gamma_L^{(1)} + 5\right]h^3\frac{\partial^4 H^{(1)}}{\partial z^4}\bigg|_{z_{\text{pec}}^{(1)}} + \mathcal{O}(h^4), \tag{16}$$

and the local truncation error can be expected to behave as a third-order approximation with the error vanishing when $\gamma_L^{(1)}$ approaches zero.

As similar analysis for Eq. (9) yields

$$\tau_{1/2}^{(1)} = -\frac{1}{24}\left[12\left(\gamma_L^{(1)}\right)^2 + 6\gamma_L^{(1)} - 1\right]h^2\frac{\partial^3 E^{(1)}}{\partial z^3}\bigg|_{z_{\text{pec}}^{(1)}} + \mathcal{O}(h^3). \tag{17}$$

The local truncation error on the H component, updated using Eq. (10), is straightforwardly given as

$$\tau_{N-\frac{1}{2}}^{(2)} = \frac{\gamma_R^{(2)} - 1}{4}h\frac{\partial^2 E^{(2)}}{\partial z^2}\bigg|_{z_{N-\frac{1}{2}}^{(2)}} + \frac{1}{24}\left[4\left(\gamma_R^{(2)}\right)^2 - 2\gamma_R^{(2)} + 1\right]h^2\frac{\partial^3 E^{(2)}}{\partial z^3}\bigg|_{z_{N-\frac{1}{2}}^{(2)}} + \mathcal{O}(h^3), \tag{18}$$

indicating a local $\mathcal{O}(h)$ convergence which is sufficient to guarantee global $\mathcal{O}(h^2)$. However, exploiting the properties of the fields, Eq. (15), we can estimate the spatial derivatives close

to the boundaries as

$$\left.\frac{\partial^2 E^{(2)}}{\partial z^2}\right|_{z^{(2)}_{N-\frac{1}{2}}} = \left.\frac{\partial^2 E^{(2)}}{\partial z^2}\right|_{z^{(2)}_{\text{pec}}} - \gamma_R^{(2)} h \left.\frac{\partial^3 E^{(2)}}{\partial z^3}\right|_{z^{(2)}_{\text{pec}}} + \mathcal{O}(h^2),$$

which, directly inserted into Eq. (18) and using Eq. (15), yields

$$\tau^{(2)}_{N-\frac{1}{2}} = -\frac{1}{24}\left[8\left(\gamma_R^{(2)}\right)^2 + 4\gamma_R^{(2)} - 1\right] h^2 \left.\frac{\partial^3 E^{(2)}}{\partial z^3}\right|_{z^{(2)}_{\text{pec}}} + \mathcal{O}(h^3). \tag{19}$$

Hence, the local truncation error near the PEC boundary is at least second order. We note in particular that for $\gamma_R^{(2)} = 0$, the internal staggered scheme is recovered.

In light of the estimates summarized in Eqs. (16)–(19), the scheme can be expected to be globally second-order accurate and with the error being only weakly dependent on the values of $\gamma^{(k)}$ close to a PEC wall. As we shall see in Section 2.4, these conclusions can be verified through computational experiments.

Prior to that, however, let us also consider the error associated with the treatment of the material interfaces. Considering the scheme for updating $H^{(1)}_{N-\frac{1}{2}}$, as given in Eq. (12), we recover

$$\begin{aligned}\mu^{(1)} \frac{dH^{(1)}_{N-\frac{1}{2}}}{dt} &= \frac{2}{2\gamma_R^{(1)} + 1} \frac{E_{\text{mat}} - E^{(1)}_{N-1}}{h} \\ &= \frac{2}{\left(2\gamma_R^{(1)} + 1\right)h}\left[E^{(2)}_0 - E^{(1)}_{N-1} + \frac{1}{2}\left(2\gamma_R^{(1)} + 1\right)\left(E^{(2)}_1 - E^{(2)}_0\right)\right],\end{aligned}$$

by combining Eqs. (11) and (12) with the relation $\gamma_L^{(2)} = \frac{1}{2} - \gamma_R^{(1)}$. To derive an expression through the usual techniques of Taylor expansions, one has to exercise some caution because the solution, while it exists, generally cannot be assumed to be smooth across the material interface. The only information that is available is given in Eq. (3), i.e., the field components are continuous across the interface.

With this in mind we shall do the error analysis at the grid points using solutions at the material interface positioned at z_{mat}. Carefully keeping track of the one-sided derivatives, one obtains

$$\tau^{(1)}_{N-\frac{1}{2}} = \frac{2\gamma_R^{(1)} - 1}{4} h \left.\frac{\partial^2 E^{(1)}}{\partial z^2}\right|_{z^-_{\text{mat}}} + \frac{\left(2\gamma_R^{(1)} - 1\right)\left(3 - 2\gamma_R^{(1)}\right)}{4\left(2\gamma_R^{(1)} + 1\right)} h \left.\frac{\partial^2 E^{(2)}}{\partial z^2}\right|_{z^+_{\text{mat}}} + \mathcal{O}(h^2), \tag{20}$$

as the leading term in the local truncation error. Here z^-_{mat} and z^+_{mat} refers to one-sided derivatives from the left and the right of the material interface, respectively. We note that the local truncation error is of $\mathcal{O}(h)$ which is sufficient to guarantee global second-order convergence [21]. Moreover, we also observe that for $\gamma_R^{(1)} = \frac{1}{2}$, the whole first-order contribution vanishes, and the standard staggered grid truncation error is recovered.

The analysis of the scheme, shown in Eq. (14), for updating $E_0^{(2)}$ proceeds along the same lines, yielding a local truncation error of the form

$$\tau_0^{(2)} = -\frac{2\gamma_L^{(2)}-1}{4}h\frac{\partial^2 H^{(2)}}{\partial z^2}\bigg|_{z_{\text{mat}}^+} - \frac{\left(2\gamma_L^{(2)}-1\right)\left(3-2\gamma_L^{(2)}\right)}{4\left(2\gamma_L^{(2)}+1\right)}h\frac{\partial^2 H^{(1)}}{\partial z^2}\bigg|_{z_{\text{mat}}^-} + \mathcal{O}(h^2), \tag{21}$$

in which we again establish local first-order behavior and recovery of the standard scheme for $\gamma_L^{(2)} = \frac{1}{2}$. One should keep in mind, however, that $\gamma_L^{(2)} + \gamma_R^{(1)} = \frac{1}{2}$, i.e., they can never both vanish, and a first-order error term of the type given in Eqs. (20) and (21) will always be present and will, in light of the analysis for the errors at the PEC wall, be the dominant source of error.

2.3. Stability and Convergence

While the issues of local and global accuracy can be addressed using standard techniques in combination with [21], the questions of stability and convergence are considerably more complex because of the extensive use of one-sided stencils and extrapolations in combination with a variable position of the interfaces.

To address this critical issue, let us rewrite Eq. (1) in symmetric form

$$\begin{aligned}\frac{\partial \hat{E}^{(k)}}{\partial t} &= c^{(k)}\frac{\partial \hat{H}^{(k)}}{\partial z},\\ \frac{\partial \hat{H}^{(k)}}{\partial t} &= c^{(k)}\frac{\partial \hat{E}^{(k)}}{\partial z},\end{aligned} \tag{22}$$

where, as compared to Eq. (1), we have normalized the field components as

$$\hat{E}^{(k)} = \frac{\varepsilon^{(k)}}{\sqrt{\mu^{(k)}}}E^{(k)}, \quad \hat{H}^{(k)} = \sqrt{\varepsilon^{(k)}}H^{(k)}, \quad c^{(k)} = \frac{1}{\sqrt{\varepsilon^{(k)}\mu^{(k)}}},$$

representing the normalized fields in the k-th region and the normalized speed of light in the material, respectively. For simplicity, we shall restrict the attention to the nonmagnetic case of $\mu^{(1)} = \mu^{(2)} = 1$.

The fields are collocated at the staggered grid, Eq. (4), and, similar to the situation shown in Fig. 2, we assume that the first grid point on the left is an electric point and that the last point on the right is a magnetic point.

Let us introduce the projection of the exact solution, $\boldsymbol{u}$, onto the grid in the form of a grid vector sorted as

$$\boldsymbol{u} = \left[\hat{E}_0^{(1)}, \hat{H}_{\frac{1}{2}}^{(1)}, \ldots, \hat{E}_{N-1}^{(1)}, \hat{H}_{N-\frac{1}{2}}^{(1)}, \hat{E}_0^{(2)}, \hat{H}_{\frac{1}{2}}^{(2)}, \ldots, \hat{E}_{N-1}^{(2)}, \hat{H}_{N-\frac{1}{2}}^{(2)}\right]^T. \tag{23}$$

Using this, we write Eq. (22) in the semi-discrete matrix form

$$\frac{d\boldsymbol{u}}{dt} = \mathrm{M}\boldsymbol{u} + \boldsymbol{T}, \tag{24}$$

where $\boldsymbol{T}$ represents the grid vector of the local pointwise truncation error, and the matrix, M, has the general structure

$$\mathrm{M} = \frac{1}{h}\left[\begin{array}{c|c|c} \mathrm{M}^L & c^{(1)} \; 0 & 0 \\ \hline 0 \quad -c^{(1)} & \mathrm{M}^M & c^{(2)} \; 0 \\ \hline 0 & 0 \quad -c^{(2)} & \mathrm{M}^R \end{array}\right]. \tag{25}$$

The three nonzero blocks, $\mathrm{M}^L, \mathrm{M}^M$, and M^R, are generated directly from the stencils introduced in Section 2.1, i.e., M^L is antisymmetric Toeplitz, representing the inner scheme of Eqs. (6) and (7), except for a 4×4 block in the upper left corner to account for the scheme given by Eqs. (8) and (9). Similarly, M^R is antisymmetric Toeplitz except for a 2×2 block in the right lower corner, representing the modifications given by Eq. (10). The remaining block, M^M, is a bit more complex, as it contains all the elements accounting for the extrapolations given in Eq. (11) and Eq. (13), and the special differences used to update $H^{(1)}_{N-\frac{1}{2}}$ and $E^{(2)}_0$, given in Eq. (12) and Eq. (14), respectively. Hence, M^M has a central 6×6 block and tridiagonal antisymmetric Toeplitz-like bands above and below the central block. The exact entries of the three M-submatrices are given in the Appendix.

While $\boldsymbol{u}$ represents the projection of the exact solution, we may also consider the grid-vector, $\boldsymbol{v}$, ordered as $\boldsymbol{u}$, as the solution to the semi-discrete problem, i.e., $\boldsymbol{v}$ satisfies

$$\frac{d\boldsymbol{v}}{dt} = \mathrm{M}\boldsymbol{v},$$

subject to the same set of initial and boundary conditions as $\boldsymbol{u}$. If we introduce the grid vector, $\boldsymbol{\epsilon} = \boldsymbol{u} - \boldsymbol{v}$, as a measure of the pointwise error, $\boldsymbol{\epsilon}$, satisfies the error equation

$$\frac{d\boldsymbol{\epsilon}}{dt} = \mathrm{M}\boldsymbol{\epsilon} + \boldsymbol{T}. \tag{26}$$

Clearly, $\boldsymbol{\epsilon}$ is subject to homogeneous initial and boundary conditions.

Let us now assume that M is similar to an antisymmetric matrix, A, as

$$\mathrm{M} = \mathrm{Q}^{-1}\mathrm{A}\mathrm{Q},$$

uniformly in h, $\gamma_L^{(k)}$, and $\gamma_R^{(k)}$. Hence, $\|\mathrm{Q}\|_h$ and $\|\mathrm{Q}^{-1}\|_h$ are bounded as h approaches zero and for all permissible values of $\gamma_L^{(k)}$, and $\gamma_R^{(k)}$.

Here, and in the following, we shall use the familiar definitions of the discrete inner products and norms

$$(\boldsymbol{u}, \boldsymbol{v})_h = h\sum_j u_j v_j, \quad \|\boldsymbol{u}\|_h = (\boldsymbol{u}, \boldsymbol{u})_h^{1/2}, \quad \|\mathrm{Q}\|_h = \sup_{\|u\|_h \neq 0} \frac{\|\mathrm{Q}\boldsymbol{u}\|_h}{\|\boldsymbol{u}\|_h}.$$

Let us furthermore assume that there exists two nonnegative constants, k_1 and k_2, such that

$$k_1^2\|\boldsymbol{u}\|_h^2 \leq (\boldsymbol{u}, \mathrm{H}\boldsymbol{u})_h \leq k_2^2\|\boldsymbol{u}\|_h^2,$$

where we have introduced the symmetric matrix, $\mathrm{H} = \mathrm{Q}^T\mathrm{Q}$. In other words, the H-norm, $\|\boldsymbol{u}\|_H^2 = (\boldsymbol{u}, \mathrm{H}\boldsymbol{u})_h$, is assumed to be equivalent to the discrete L^2-norm, $\|\boldsymbol{u}\|_h^2$. We note that an immediate consequence of this is that $\|\mathrm{Q}^{-1}\|_h$ is bounded if $\|\mathrm{Q}\|_h$ is bounded.

In this setting, Eq. (26) yields

$$\frac{1}{2}\frac{d}{dt}(\boldsymbol{\epsilon}, \mathrm{H}\boldsymbol{\epsilon})_h = \frac{1}{2}\frac{d}{dt}\|\boldsymbol{\epsilon}\|_H^2 = (\boldsymbol{\epsilon}, \mathrm{Q}^T\mathrm{AQ}\boldsymbol{\epsilon})_h + (\boldsymbol{\epsilon}, \mathrm{Q}^T\mathrm{Q}\boldsymbol{T})_h.$$

As $\mathrm{Q}^T\mathrm{AQ}$ is antisymmetric, the Cauchy–Schwarz inequality immediately implies

$$\frac{1}{2}\frac{d}{dt}\|\boldsymbol{\epsilon}\|_H \leq \|\boldsymbol{T}\|_H,$$

which, after integration in time, yields

$$\|\boldsymbol{\epsilon}\|_H \leq \int_0^t \|\boldsymbol{T}(s)\|_H \, ds.$$

From the L^2 equivalence of the H-norm we finally recover that there exists a constant, K, such that

$$\|\boldsymbol{\epsilon}\|_h \leq \frac{k_2}{k_1} \max_{s\in[0,t]} \|\boldsymbol{T}(s)\|_h t \leq Kt,$$

i.e., the error can grow, at most, linearly in time.

We have thus established the following general convergence result [23, 24].

LEMMA 2.1 *If the matrix* M *in Eq.* (24) *is uniformly similar to an antisymmetric matrix,* $A = QMQ^{-1}$, *and* $\|Q\|_h\|Q^{-1}\|_h$ *is uniformly bounded for all values of* h, $\gamma_L^{(k)}$, *and* $\gamma_R^{(k)}$, *then there exists a constant,* K, *such that the error,* $\boldsymbol{\epsilon}$, *is bounded as*

$$\|\boldsymbol{\epsilon}\|_h \leq Kt,$$

where K *can be a function of* h *and* u *but not of* t.

Such a scheme is termed a bounded error scheme.

Provided the scheme is consistent, i.e., $\|\boldsymbol{T}\|_h$ is at least $\mathcal{O}(h)$, establishing error-boundedness of a particular scheme is clearly a stronger statement than proving convergence using the Lax equivalence theorem, which allows up to exponential growth in time. Moreover, if the scheme is bounded error according to Lemma 2.1, von Neumann stability is sufficient for fully discrete stability [22], i.e., we can find a strict bound on the maximum time-step by bounding the eigenvalues, $|\lambda_m|$, of M.

In the following we shall pursue these two avenues, establishing semi-discrete as well as conditional fully discrete stability of the scheme given in Eqs. (6)–(14).

2.3.1. Semi-discrete stability and convergence. While we shall leave all the details of the proof of the bounded error property of the scheme in Eqs. (6)–(14) to the Appendix, it shall prove illustrative to sketch the main ideas. The proof is constructive and is based on the construction of an antisymmetric matrix, A, which is similar to M as

$$\mathrm{M} = \mathrm{Q}^{-1}\mathrm{AQ},$$

and $\|\mathrm{Q}^{-1}\|_h \|\mathrm{Q}\|_h \leq C$, i.e., if Q and its inverse are nonsingular and uniformly bounded in the h-norm, then the conditions of Lemma 2.1 are fulfilled, and the scheme is a bounded error scheme.

To construct the matrix A, we first note that since it should be valid for an arbitrary number of interior grid points in each region, it is natural to expect that it will have a global structure similar to that of M, i.e.,

$$\mathrm{A} = \frac{1}{h}\left[\begin{array}{c|c|c} \mathrm{A}^L & c^{(1)} \; 0 & 0 \\ \hline 0 \; -c^{(1)} & \mathrm{A}^M & c^{(2)} \; 0 \\ \hline 0 & 0 \; -c^{(2)} & \mathrm{A}^R \end{array}\right]. \tag{27}$$

Moreover, we assume that the structure of the three submatrices, A^L, A^M, and A^R, are as discussed for M^L, M^M, and M^R. To prove that A and M have the same eigenvalue spectrum, one can exploit the Toeplitz-like structure of the submatrices to develop recurrence relations for the characteristic polynomials. In that way, one need only prove that the initial characteristic polynomials, caused by the modified terms, are identical to establish that A and M have the same characteristic polynomial and, hence, the same eigenvalue spectrum. The specification of A is by construction, and the entries are given in the Appendix.

To establish the existence of a nonsingular similarity transform we consider

$$\mathrm{QM} = \mathrm{AQ}.$$

As in the case of A, it is natural, although not necessary, to require that Q takes the global form

$$\mathrm{Q} = \left[\begin{array}{c|c|c} \mathrm{Q}^L & -q^{(1)} \; 0 & 0 \\ \hline 0 \; q^{(1)} & \mathrm{Q}^M & -q^{(2)} \; 0 \\ \hline 0 & 0 \; q^{(2)} & \mathrm{Q}^R \end{array}\right]. \tag{28}$$

Again, the structure of the three submatrices, Q^L, Q^M, and Q^R, are as discussed for M^L, M^M, and M^R, with the main difference being that the diagonal terms are nonzero, and that $q^{(k)}$ are different from the local speed of light. The exact entries of Q are given in the Appendix.

To prove that Q is nonsingular and $\|\mathrm{Q}^{-1}\|_h \|\mathrm{Q}\|_h \le C$, it suffices to prove that the H-norm, with $\mathrm{H} = \mathrm{Q}^T\mathrm{Q}$ is L^2-equivalent. This, however, follows directly from the expression for Q given in Appendix since

$$\begin{aligned} k_1^2 = \frac{\min\left\{c^{(1)^2}, c^{(1)^2}\right\}}{4} &\le \frac{1}{4}\left(\mathbf{u},\ \mathrm{diag}\left(c^{(1)^2}, \ldots, c^{(1)^2}, c^{(2)^2}, \ldots, c^{(2)^2}\right)\mathbf{u}\right)_h \\ &\le (\mathbf{u},\ Q^T Q\mathbf{u})_h \\ &\le 4\left(\mathbf{u},\ \mathrm{diag}\left(c^{(1)^2}, \ldots, c^{(1)^2}, c^{(2)^2}, \ldots, c^{(2)^2}\right)\mathbf{u}\right)_h \\ &\le 4\max\left\{c^{(1)^2}, c^{(1)^2}\right\} = k_2^2; \quad \|\mathbf{u}\|_h = 1. \end{aligned}$$

Through this line of arguments, we can thus establish Theorem 2.1.

THEOREM 2.1. *The scheme proposed in Eqs.* (6)–(14) *is an bounded error scheme and therefore it is stable.*

Proof. This follows immediately since

$$M = Q^{-1} A Q,$$

where $A = -A^T$, and $\|\mathrm{Q}\|_h \|\mathrm{Q}^{-1}\|_h \leq C$ since $k_1 \leq \|\mathrm{Q}\|_h \leq k_2$.

Following Lemma 2.1, the scheme is a bounded error scheme. ∎

Before considering the fully discrete stability, it is worth realizing a few things. In particular, we note that the proof of stability is for the general case of two arbitrary materials, connected at an interface exactly as sketched in Fig. 2. However, to prove stability for the more general case of a sequence of material interfaces one can apply a similar constructive approach involving the recurrence relations of the characteristic polynomials and the determinants sequentially.

Let us finally consider the case in which E or H is not continuous across the material interface. While this is unphysical for the purely one-dimensional case, it is a situation that appears frequently in the general multidimensional case, as we shall discuss further in Section 3.

Without loss of generality, we can consider a situation in which the magnetic field components remain continuous but the electric field components are related as

$$E^{(1)} = \phi\big(\varepsilon^{(1)}, \varepsilon^{(2)}\big) E^{(2)}.$$

This immediately suggests that such a situation can be dealt with by simply modifying the computation of E_{mat} in Eq. (11) by multiplication with $\phi(\varepsilon^{(1)}, \varepsilon^{(2)})$ before being introduced into Eq. (12) for the update of $H^{(1)}_{N-1/2}$. We shall return to the performance of this approach in Section 3.3.

To appreciate the validity of the stability proof under such slightly changed circumstances, it suffices to recall that by proving boundedness of the error we establish convergence of the approximation directly. Since the approximation satisfies the jump-condition to the order of the scheme, one is left with the same error-equation, Eq. (26), that was proven to be bounded error in the above, hence establishing convergence for the generalized case.

Another way of realizing a similar result is to exploit the multidomain nature of the scheme, i.e., if the solutions in each of the regions are well behaved one could view the interface as connecting two separate problems through a set of given conditions. As long as these conditions are reasonable, e.g. bounded and smooth, one should expect that they all lead to stable approximations. This also suggests that one could introduce an artificial interface in a homogeneous region as part of a multidomain scheme to enhance parallel efficiency, among other things.

2.3.2. Fully discrete stability. While semi-discrete stability is a necessary condition for fully discrete stability, it is certainly not sufficient. Establishing conditions under which a fully discrete scheme is stable is, in most cases, very painful and often impossible. However, in this particular case it is straightforward if one recalls that

$$\mathrm{M} = \mathrm{Q}^{-1}\mathrm{A}\mathrm{Q} = \mathrm{Q}^{-1}\mathrm{U}^{-1}\Lambda\mathrm{U}\mathrm{Q},$$

where $\|\mathrm{U}\|_h = \|\mathrm{U}^{-1}\|_h = 1$ since $\mathrm{A} = -\mathrm{A}^T$ and $\|\mathrm{Q}\|_h \|\mathrm{Q}^{-1}\|_h \leq C$ as established in Theorem 2.1. Hence, to ensure fully discrete stability, von Neumann stability is sufficient [22], and we only need derive a bound on the magnitude of the eigenvalues to obtain a necessary and sufficient CFL condition.

Moreover, as A is normal, its eigenvectors are orthogonal and one can estimate the magnitude of the eigenvalue $\lambda_{\max}$ as

$$|\lambda_{\max}| = |\langle \mathbf{u}_{\max}, \lambda_{\max}\, \mathbf{u}_{\max}\rangle| = |\langle \mathbf{u}_{\max}, A\, \mathbf{u}_{\max}\rangle|, \tag{29}$$

where the entries of A are given in the Appendix, and $\mathbf{u}_{\max}$ refers to the right eigenvector associated with the maximum eigenvalue.

This yields a bound for the maximum eigenvalue as

$$|\lambda_{\max}| \leq \frac{1}{h}\left[3c^{(1)} + (1+2\sqrt{2})c^{(2)}\right] \leq (4+2\sqrt{2})\frac{\max\left(c^{(1)}, c^{(2)}\right)}{h}, \tag{30}$$

for all values of $\gamma^{(k)}$. Restricting the attention to the situation with no material interface but solely metallic boundaries, one obtains the bound

$$|\lambda_{\max}| \leq 2\frac{c}{h}, \tag{31}$$

where $c = c^{(1)} = c^{(2)}$ for all positions of the metallic wall.

Numerical tests confirm that the latter bound is sharp while the former bound is very conservative and a more reasonable bound is

$$|\lambda_{\max}| \leq \frac{13}{5}\frac{\max\left(c^{(1)}, c^{(2)}\right)}{h},$$

which is only slightly above the purely metallic case.

Keeping in mind that the Yee scheme in the current setting will result in a bound as

$$\left|\lambda_{\max}^{\text{Yee}}\right| \leq 2\frac{\max\left(c^{(1)}, c^{(2)}\right)}{h},$$

we see that the time-step is only very slightly affected by the special treatment of the material interfaces, while the special treatment of metallic interfaces can be done at no penalty on the maximum stable time step.

If we term the maximum local speed of light, $c_{\max} = \max(c^{(k)})$, in any of the k regions, we have the general CFL conditions as

$$\Delta t \leq \alpha\frac{5}{13c_{\max}}h, \tag{32}$$

where $\alpha = 1$, $\alpha = \sqrt{3}$, and $\alpha = \sqrt{8}$ when using a Leapfrog scheme, a third-order or a fourth-order Runge–Kutta scheme, respectively. Note, that if staggering in time is used in connection with the Leapfrog scheme, $\alpha = 2$.

2.4. A Few Numerical Tests

To verify the analysis of the previous sections, let us consider a simple test case consisting of a one-dimensional electromagnetic resonator with perfectly conducting walls located at $z_{\text{pec}}^{(1)} = -1$ and $z_{\text{pec}}^{(2)} = 1$. The interior of the resonator can either be air-filled or be filled with two di-electric media with the material interface at $z_{\text{mat}} = 0$ and $\mu^{(1)} = \mu^{(2)} = 1.0$.

The exact solution to Eq. (1) in such a geometry, with $k = 1, 2$ signifying each of the two regions, is given as

$$E^{\mathbf{e}} = \left[A^{(k)} e^{in^{(k)}\omega z} - B^{(k)} e^{-in^{(k)}\omega z}\right] e^{i\omega t}, \tag{33}$$

and

$$H^{\mathbf{e}} = n^{(k)}\left[A^{(k)} e^{in^{(k)}\omega z} + B^{(k)} e^{-in^{(k)}\omega z}\right] e^{i\omega t}, \tag{34}$$

where

$$A^{(1)} = \frac{n^{(2)}\cos\left(n^{(2)}\omega\right)}{n^{(1)}\cos\left(n^{(1)}\omega\right)}, \quad A^{(2)} = e^{-i\omega(n^{(1)}+n^{(2)})},$$

and

$$B^{(1)} = A^{(1)} e^{-i2n^{(1)}\omega}, \quad B^{(2)} = A^{(2)} e^{i2n^{(2)}\omega}.$$

Here $n^{(k)} = \sqrt{\varepsilon^{(k)}}$ (see Fig. 2) represents the local index of refraction, and the wavenumber, ω, takes the value of $\omega = 2\pi/n$ if $n^{(1)} = n^{(2)} = n$ or is found as the solution to the equation

$$-n^{(2)}\tan\left(n^{(1)}\omega\right) = n^{(1)}\tan\left(n^{(2)}\omega\right),$$

when the cavity is filled with two different media.

For $n^{(1)} = n^{(2)}$, the solution simply represents standing sinusoidal waves while the situation is a little more complicated when $n^{(1)} \neq n^{(2)}$. As an example we show the solution for $n^{(1)} = 1$ and $n^{(2)} = 1.5$ in Fig. 3. We note in particular that the solution loses smoothness right at the material interface, $z_{\text{mat}} = 0$.

We shall seek the numerical solution to the cavity problem on the staggered grid, given in Eq. (4). Note that for $\gamma = 0$ the grid coincides with the boundaries as well as the material interface at $z_{\text{mat}} = 0$, while for $\gamma > 0$ the whole grid is shifted toward the right, creating a situation exactly as sketched in Figs. 1 and 2, with $\gamma_L^{(k)} = \gamma$ and $\gamma_R^{(k)} = \frac{1}{2} - \gamma$.

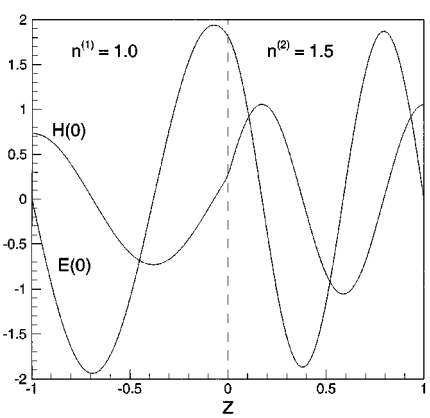

FIG. 3. Solution at $t = 0$ for a metallic cavity filled with two different materials with an interface at $z = 0$.

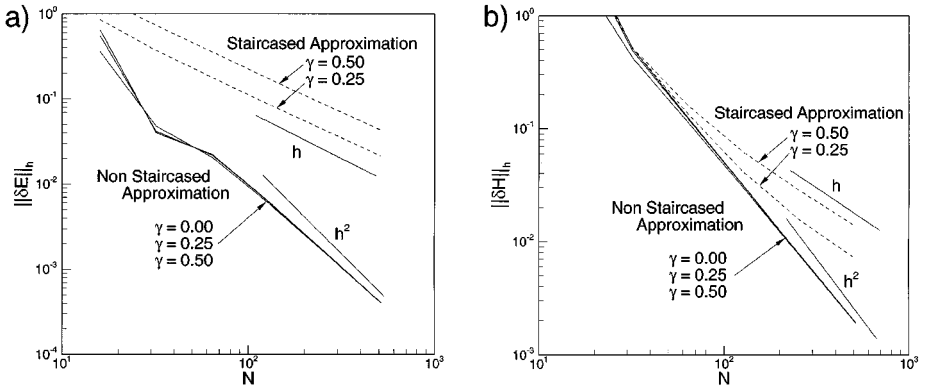

FIG. 4. The discrete L^2-error at $t = 2\pi$ for the electric (a) and the magnetic (b) field components in an air-filled metallic cavity as a function of the resolution $h = 2/N$. The dashed curves are obtained without properly accounting for the correct position of the metallic walls while the full curves are obtained with the new scheme.

Let us begin by considering the vacuum filled cavity, i.e., $n^{(1)} = n^{(2)} = 1.0$. In Fig. 4 we plot the global error at $t = 2\pi$ as a function of $N = 2/h$ for various values of γ. The measure of error is defined as

$$\|\delta E\|_h = \left(h \sum_{j=0}^{N} \left(E_j - E^{\mathbf{e}}(z_j) \right)^2 \right)^{1/2},$$

and

$$\|\delta H\|_h = \left(h \sum_{j=0}^{N-1} \left(H_{j+\frac{1}{2}} - H^{\mathbf{e}}\left(z_{j+\frac{1}{2}}\right) \right)^2 \right)^{1/2},$$

where $E^{\mathbf{e}}$ and $H^{\mathbf{e}}$ are given in Eqs. (33) and (34).

As discussed in Section 2.2, the classic staggered scheme and the new scheme are equivalent for the perfectly conducting homogeneous cavity with $\gamma = 0$, and we observe, as expected, a global $\mathcal{O}(h^2)$ convergence in Fig. 4 for both the E and the H component. However, for $\gamma > 0$, the schemes yield very different results with the classic scheme being reduced to $\mathcal{O}(h)$ convergence as a direct result of the geometry of the actual problem being approximated to first order only. The new scheme, however, maintains second-order global convergence for both field components, yielding a dramatic improvement in accuracy at no additional computational cost compared to the classical scheme. In particular, both computations use the same time step, Δt. In accordance with the analysis of Section 2.2 we observe very little change of the global error, as γ is varied.

The situation for a metallic cavity filled with two different materials, having $n^{(1)} = 1.0$ and $n^{(2)} = 1.5$, is even more alarming when one considers the performance of the classic Yee scheme. In Fig. 5 we show the decay of the global error with increasing resolution when using the staircased approximation as well as the new scheme where no staircasing is introduced. We note in particular that even when the grid is aligned with the geometry, the staircased approximation is reduced to a first-order scheme at best. The reason for this is to be found in the assumption, underlying the finite-difference approximation, that the

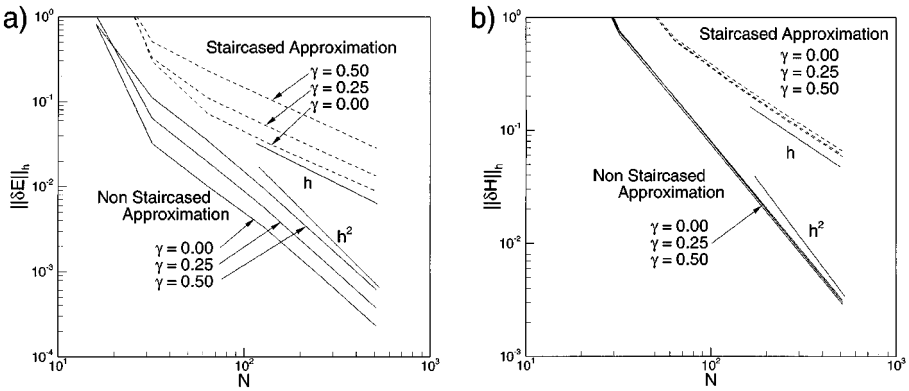

FIG. 5. The discrete L^2-error at $t = 2\pi$ for the electric (a) and the magnetic (b) field components in a metallic cavity as a function of the resolution $h = 2/N$. The cavity is filled with two materials with the interface being positioned at $z = 0$. The dashed curves are obtained without properly accounting for the position of the interfaces and the correct jump conditions while the full curves is obtained using the new scheme.

function locally can be well approximated by a second-order polynomial. While this is true in the interior of each region, the field components can only be assumed to be continuous across the material interface. Hence, in the notation of Fig. 2, updating $H^{(1)}_{N-\frac{1}{2}}$ as

$$\mu^{(1)} \frac{dH^{(1)}_{N-\frac{1}{2}}}{dt} = \frac{E^{(2)}_0 - E^{(1)}_{N-1}}{h},$$

yields a local truncation error of the form

$$\tau^{(1)}_{N-\frac{1}{2}} = \frac{E^{(2)}(z^+_{\text{mat}}) - E^{(1)}(z^-_{\text{mat}})}{h} + \gamma \left(\frac{\partial E^{(2)}}{\partial z}\bigg|_{z^+_{\text{mat}}} - \frac{\partial E^{(1)}}{\partial z}\bigg|_{z^-_{\text{mat}}} \right) + \frac{\gamma^2}{2} h \left(\frac{\partial^2 E^{(2)}}{\partial z^2}\bigg|_{z^+_{\text{mat}}} - \frac{\partial^2 E^{(1)}}{\partial z^2}\bigg|_{z^-_{\text{mat}}} \right) + \mathcal{O}(h^2), \tag{35}$$

and similarly for $E^{(2)}_0$. In situations in which the field components can be assumed to be continuous, one recovers a locally constant term, implying that first-order global convergence can be expected [21]. Note that this is true for all values of γ, as is confirmed in Fig. 5. This is consistent with the analysis of [10, 19], showing that the global error is $\mathcal{O}(h)$ in the general case.

The above result, however, has a more serious consequence for situations in which the field components cannot be assumed continuous, as is the case for problems beyond one dimension. In this case, a diverging term is introduced, which may lead to the formation of spurious nonvanishing solutions. We shall return to a more detailed discussion of this in Section 3.

For the new scheme, where no implicit assumptions are made about the behavior of the field components when they pass the material interface, the situation is significantly better, even for a grid aligned with the problem, i.e., $\gamma = 0$. As shown in Fig. 5, the global second-order convergence is recovered for all values of γ, confirming the analysis of Section 2.2.

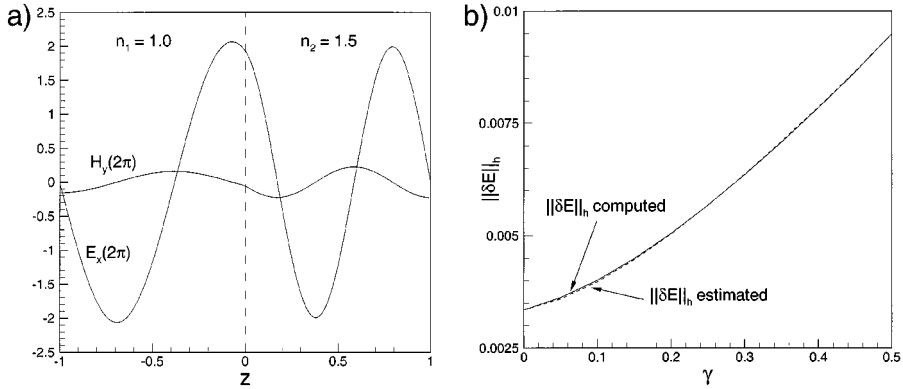

FIG. 6. In a) we show the solution at $t = 2\pi$ for a cavity filled with two materials with the interface being positioned at $z = 0$, while b) shows the γ-dependence of $\|\delta E\|_h$ as computed (full line) and estimated (dashed line) using the results of the error analysis.

The analysis also suggested that the error could be expected to depend on the actual value of γ—a fact that is clearly reflected in $\|\delta E\|_h$ and less so for $\|\delta H\|_h$ in Fig. 5. To understand this, and come to an appreciation of the validity of the error analysis of Section 2.2, we show in Fig. 6 the solution at $t = 2\pi$. In particular, one observes that the magnitude of E is larger than H, explaining the higher absolute error level of $\|\delta H\|_h$ through the use of Eq. (20). A closer inspection indeed reveals that the absolute variation of $\|\delta H\|_h$ is approximately the same as for $\|\delta E\|_h$.

A more quantitative test of the validity of the error analysis is also illustrated in Fig. 6 in which we plot the computed global error $\|\delta E\|_h$ as a function of γ. Based on the estimate in Eq. (21) one should expect the dominant error term to depend on γ as

$$\|\delta E\|_h \sim a\gamma + b + c\frac{(2\gamma - 1)(3 - 2\gamma)}{2\gamma + 1},$$

where a, b, and c are time-dependent parameters. Computing these parameters for the present problem at $t = 2\pi$, we show in Fig. 6 the variation of the estimated $\|\delta E\|_h$ compared to the computed error as a function of γ, yielding an excellent agreement and giving confidence in the analysis and in the conclusions we have based on it.

3. BEYOND ONE DIMENSION

In the previous section we focused on the details of the new scheme in a one-dimensional setting. However, as we shall discuss in the following and subsequently illustrate, the general ideas underlying the new scheme extends to two- and three-dimensional problems, provided only that special attention is paid to the boundary conditions at PEC boundaries and at material interfaces. The reason additional work is needed for problems beyond one dimension is the introduction of a new physical phenomenon: the individual field components become discontinuous.

3.1. Specific Multidimensional Concerns

As the treatment of the interfaces is a little different depending on the various cases, we find it illustrative to discuss the two-dimensional equations prior to addressing the general three-dimensional scenario. However, because of the variation of the problems we shall not attempt to account for all possible situations but rather present the general ideas underlying the extension of the one-dimensional approach to a multidimensional scenario.

3.1.1. The two-dimensional equations. Let us begin by considering the two-dimensional TM equations for (H^z, H^x, E^y) on the form

$$\begin{aligned} \mu \frac{\partial H^z}{\partial t} &= -\frac{\partial E^y}{\partial x}, \\ \mu \frac{\partial H^x}{\partial t} &= \frac{\partial E^y}{\partial z}, \\ \varepsilon \frac{\partial E^y}{\partial t} &= \frac{\partial H^x}{\partial z} - \frac{\partial H^z}{\partial x}. \end{aligned} \tag{36}$$

The field components, $(H^{z,(k)}, H^{x,(k)}, E^{y,(k)})$, are subject to boundary conditions between two regions, with material parameters, $\varepsilon^{(k)}$ and $\mu^{(k)}$, for $k = 1, 2$, as

$$\hat{\boldsymbol{n}} \times \boldsymbol{H}^{(1)} = \hat{\boldsymbol{n}} \times \boldsymbol{H}^{(2)}, \tag{37}$$

$$\mu^{(1)} \hat{\boldsymbol{n}} \cdot \boldsymbol{H}^{(1)} = \mu^{(2)} \hat{\boldsymbol{n}} \cdot \boldsymbol{H}^{(2)}, \tag{38}$$

$$E^{y,(1)} = E^{y,(2)}. \tag{39}$$

Here $\boldsymbol{H}^{(k)} = (H^{z,(k)}, H^{x,(k)}, 0)^T$ and $\hat{\boldsymbol{n}} = (\hat{n}_z, \hat{n}_x, 0)^T$ represents a unit vector normal to the interface.

Let us note that when considering a nonmagnetic media, i.e., $\mu^{(1)} = \mu^{(2)} = 1.0$, Eqs. (37) and (38) imply that each of the individual components of $\boldsymbol{H}$ be continuous across the interface. In this particularly simple case, the one-dimensional scheme generalizes straightforwardly by applying it dimension by dimension, as each individual field component remains continuous across the boundary.

For the more general case of $\mu^{(1)} \neq \mu^{(2)}$ more care has to be exercised. Since E^y is continuous, updating H^z and H^x follows the one-dimensional approach while updating E^y requires attention to the possibility of H^z and H^x being discontinuous across the interface.

Let us, as an example, consider the scenario in Fig. 7. As usual, we have introduced the two-dimensional staggered grid constructed from the tensor-product of the grids

$$z_i = h_z i, \quad z_{i+\frac{1}{2}} = h_z\big(i + \tfrac{1}{2}\big), \quad x_j = h_x j, \quad x_{j+\frac{1}{2}} = h_x\big(j + \tfrac{1}{2}\big),$$

where h_z and h_x represent the constant grid sizes along the z and x axis. As in the one-dimensional case, the limits on j depend on the details of the actual problem. For simplicity, we assume that $h_z = h_x = h$.

The field variables are collocated as

$$H^z_{i,j+\frac{1}{2}} = H^z\big(z_i, x_{j+\frac{1}{2}}\big), \quad H^x_{i+\frac{1}{2},j} = H^x\big(z_{i+\frac{1}{2}}, x_j\big), \quad E^y_{i,j} = E^y(z_i, x_j),$$

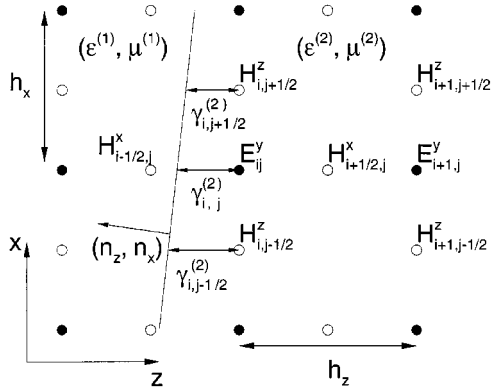

FIG. 7. Illustration of the scheme in a 2D-TM case. The full line signifies the position of the material interface.

and, following Eq. (14), we consider the computation of the z-derivative of H^x at (z_i, x_j) as

$$\frac{\partial H^x_{i,j}}{\partial z} = \frac{2}{2\gamma^{(2)}_{ij}+1}\frac{H^x_{i+\frac{1}{2},j} - H^x_{\text{mat}}}{h}. \tag{40}$$

The computation of H^x_{mat} is, however, somewhat more involved than in the one-dimensional case as the boundary conditions on the magnetic field components at the material interface take the form

$$\begin{aligned} \hat{n}_z H^{x,(1)} - \hat{n}_x H^{z,(1)} &= \hat{n}_z H^{x,(2)} - \hat{n}_x H^{z,(2)}, \\ \mu^{(1)}\big(\hat{n}_z H^{z,(1)} + \hat{n}_x H^{x,(1)}\big) &= \mu^{(2)}\big(\hat{n}_z H^{z,(2)} + \hat{n}_x H^{x,(2)}\big), \end{aligned} \tag{41}$$

i.e., there are a total of four unknowns with $H^{x,(2)} = H^x_{\text{mat}}$ being the sought after field component. The computation of $H^{x,(1)}$, however, follows directly from the one-dimensional scheme, given in Eq. (13), through an extrapolation as

$$H^{x,(1)} = \big(1+\gamma^{(1)}_{i,j}\big)H^x_{i-\frac{1}{2},j} - \gamma^{(1)}_{i,j}H^x_{i-\frac{3}{2},j}, \tag{42}$$

where $\gamma^{(1)}_{i,j} = \frac{1}{2} - \gamma^{(2)}_{i,j}$. Since we have two constraints, Eq. (41), we shall need one more variable to compute H^x_{mat}.

To minimize the error associated with the use of extrapolations we shall generally strive to design the scheme such that an extrapolation never extends beyond half a grid cell. Hence, while one could be tempted to seek an approximation to $H^{z,(1)}$ through an extrapolation similar to that for $H^{x,(1)}$, an inspection of the grid in Fig. 7 reveals that such extrapolations will extend beyond half a grid-cell and consequently be a source of significant error.

We therefore choose to estimate $H^{z,(2)}$ by first computing the two quantities

$$\tilde{H}^z_{j\pm\frac{1}{2}} = \Big(1+\gamma^{(2)}_{i,j\pm\frac{1}{2}}\Big)H^z_{i,j\pm\frac{1}{2}} - \gamma^{(2)}_{i,j\pm\frac{1}{2}}H^z_{i+1,j\pm\frac{1}{2}},$$

and subsequently approximate $H^{z,(2)}$ as

$$H^{z,(2)} = \frac{\tilde{H}^z_{j+\frac{1}{2}} + \tilde{H}^z_{j-\frac{1}{2}}}{2},$$

i.e., the material interface is assumed to be locally piecewise linear. Using Taylor expansions, one can easily show that $H^{z,(2)}$ yields an $\mathcal{O}(h)$ approximation to the true $H^{z,(2)}$, which is consistent with the other elements of the scheme.

With this, one immediately obtains

$$H^x_{\text{mat}} = H^{x,(1)} + \hat{n}_x\big(\mu^{(1)} - \mu^{(2)}\big)\frac{H^{z,(2)}\hat{n}_z + H^{x,(1)}\hat{n}_x}{\mu^{(1)}\hat{n}_z^2 + \mu^{(2)}\hat{n}_x^2}, \tag{43}$$

as a first-order approximation to the field quantity needed in Eq. (40). We note that for $\mu^{(1)} = \mu^{(2)}$ one recovers $H^x_{\text{mat}} = H^{x,(1)}$, i.e., the one-dimensional approach as discussed above.

In the event that a material interface intersects a vertical grid line, hence requiring that H^z_{mat} be computed as part of the scheme

$$\frac{\partial H^z_{i,j}}{\partial z} = \frac{2}{2\gamma^{(2)}_{i,j} + 1}\frac{H^z_{i+1,j+\frac{1}{2}} - H^z_{\text{mat}}}{h}, \tag{44}$$

a construction similar to the one used for H^x_{mat} can be applied.

It is noteworthy that the scheme for computing H^x_{mat} becomes particularly simple when $\hat{n}_x = 0$, i.e., in the case where the interface is parallel to the x-axis but not necessarily coinciding with the axis itself. The same is naturally true for H^z_{mat} in case $\hat{n}_z = 0$. In such cases the scheme reduces to the one-dimensional approach provided only that the jump-conditions are accounted for correctly. It is only in situations in which the material interface has curvature or are at some angle to the grid that the more complicated approach is required, as only in these cases are the field components discontinuous along directions in which derivatives are computed.

We shall also briefly consider the treatment of the boundary in case it is a perfect conductor. To update H^x and H^z near boundaries one can simply use the Dirichlet boundary condition as

$$E^{y,(2)} = 0. \tag{45}$$

However, as for the case in which a material is present, a little more attention is needed to update E^y in the general case. Let us, as an example, again consider the situation sketched in Fig. 7. Assuming that the intersecting boundary is metallic and only $E^y_{i,j}$ needs to be updated, we must estimate H^x_{pec} such that the z-derivative of H^x at (z_i, x_j) can be computed as

$$\frac{\partial H^x_{i,j}}{\partial z} = \frac{2}{2\gamma^{(2)}_{i,j} + 1}\frac{H^x_{i+\frac{1}{2},j} - H^x_{\text{pec}}}{h}, \tag{46}$$

subject to the boundary condition

$$\hat{n}_z H^{z,(2)} + \hat{n}_x H^{x,(2)} = 0,$$

where $H^{x,(2)} = H^x_{\text{pec}}$. In the general case in which $\hat{n}_x \neq 0$, an approximation of $H^{z,(2)}$ can be obtained exactly as in the case of the material interface as an average of $\tilde{H}^z_{j\pm\frac{1}{2}}$ computed from the interior of the domain. In the remaining case, with $\hat{n}_x = 0$ corresponding to the metallic wall being aligned vertically with the grid, the problem becomes purely one-dimensional and computing the z-derivative of H^x is done following Eq. (8) as

$$\frac{\partial H^x_{i,j}}{\partial z} = \frac{\gamma^{(2)}_{i,j}}{1+\gamma^{(2)}_{i,j}} \frac{H^x_{i+\frac{3}{2},j} - H^x_{i+\frac{1}{2},j}}{h},$$

and Eq. (9) for updating the neighboring H^x.

Let us finally briefly discuss a situation in which the TE form of Maxwell's equations, given as

$$\begin{aligned} \varepsilon \frac{\partial E^z}{\partial t} &= \frac{\partial H^y}{\partial x} \\ \varepsilon \frac{\partial E^x}{\partial t} &= -\frac{\partial H^y}{\partial z}, \\ \mu \frac{\partial H^y}{\partial t} &= \frac{\partial E^z}{\partial x} - \frac{\partial E^x}{\partial z}, \end{aligned} \tag{47}$$

is being considered. In this event, the boundary conditions between two regions with fields $(E^{z,(k)}, E^{x,(k)}, H^{y,(k)})$ and material parameters, $\varepsilon^{(k)}$ and $\mu^{(k)}$, take the form

$$\hat{\boldsymbol{n}} \times \boldsymbol{E}^{(1)} = \hat{\boldsymbol{n}} \times \boldsymbol{E}^{(2)}, \tag{48}$$

$$\varepsilon^{(1)} \hat{\boldsymbol{n}} \cdot \boldsymbol{E}^{(1)} = \varepsilon^{(2)} \hat{\boldsymbol{n}} \cdot \boldsymbol{E}^{(2)}, \tag{49}$$

$$H^{y,(1)} = H^{y,(2)}, \tag{50}$$

where $\boldsymbol{E}^{(k)} = (E^{z,(k)}, E^{x,(k)}, 0)^T$ and $\hat{\boldsymbol{n}} = (\hat{n}_z, \hat{n}_x, 0)^T$ represents a unit vector normal to the interface.

When directly comparing Eqs. (36)–(39) for the TM case with the above Eqs. (47)–(50) for the TE case, one easily realizes that the latter can be obtained from the former through the simple transformation $(\mu H^z, \mu H^x, \varepsilon E^y) \to (\varepsilon E^z, \varepsilon E^x, -\mu H^y)$. Hence, the duality of Maxwell's equations directly yields the scheme for the 2D TE case based on the 2D TM discussed in detail in the above.

3.1.2. Three-dimensional concerns. Let us also attend to a number of problems associated with the extension of the scheme to a three-dimensional situation. As for the two-dimensional case we shall not attempt to formulate schemes for all possible scenarios but rather point out the general ideas underlying the extension.

In three dimensions, Maxwell's equations take the form

$$\begin{aligned} \varepsilon \frac{\partial E^z}{\partial t} &= \frac{\partial H^y}{\partial x} - \frac{\partial H^x}{\partial y}, \quad \mu \frac{\partial H^z}{\partial t} = \frac{\partial E^x}{\partial y} - \frac{\partial E^y}{\partial x}, \\ \varepsilon \frac{\partial E^x}{\partial t} &= \frac{\partial H^z}{\partial y} - \frac{\partial H^y}{\partial z}, \quad \mu \frac{\partial H^x}{\partial t} = \frac{\partial E^y}{\partial z} - \frac{\partial E^z}{\partial y}, \\ \varepsilon \frac{\partial E^y}{\partial t} &= \frac{\partial H^x}{\partial z} - \frac{\partial H^z}{\partial x}, \quad \mu \frac{\partial H^y}{\partial t} = \frac{\partial E^z}{\partial x} - \frac{\partial E^x}{\partial z}. \end{aligned} \tag{51}$$

The fields, $\boldsymbol{E}^{(k)} = (E^{z,(k)}, E^{x,(k)}, E^{y,(k)})^T$ and $\boldsymbol{H}^{(k)} = (H^{z,(k)}, H^{x,(k)}, H^{y,(k)})^T$, in two regions of different materials, $\varepsilon^{(k)}$ and $\mu^{(k)}$ with $k = 1, 2$, are connected as

$$\hat{\boldsymbol{n}} \times \boldsymbol{E}^{(1)} = \hat{\boldsymbol{n}} \times \boldsymbol{E}^{(2)}, \quad \varepsilon^{(1)} \hat{\boldsymbol{n}} \cdot \boldsymbol{E}^{(1)} = \varepsilon^{(2)} \hat{\boldsymbol{n}} \cdot \boldsymbol{E}^{(2)}, \tag{52}$$

$$\hat{\boldsymbol{n}} \times \boldsymbol{H}^{(1)} = \hat{\boldsymbol{n}} \times \boldsymbol{H}^{(2)}, \quad \mu^{(1)} \hat{\boldsymbol{n}} \cdot \boldsymbol{H}^{(1)} = \mu^{(2)} \hat{\boldsymbol{n}} \cdot \boldsymbol{H}^{(2)}, \tag{53}$$

where $\hat{\boldsymbol{n}} = (n_z, n_x, n_y)^T$ signifies an normal unit vector at the interface.

As for the two-dimensional case, the one-dimensional schemes can be applied directly if the material interface is straight and aligned with one of the axis. In this case, the tangential components of all field components are smooth while the normal component, which is well specified because of the simplicity of the interface, can be adjusted directly following the jump-conditions of Eqs. (52) and (53).

For the more general case of a curvilinear boundary, however, we have to take a closer look at the problem of enforcing the proper conditions on the field components across the interface. Following usual practice we assume that the field components are collocated as

$$E^z_{i+\frac{1}{2},j,k+\frac{1}{2}} = E^z\big(z_{i+\frac{1}{2}}, x_j, y_{k+\frac{1}{2}}\big), \quad E^x_{i,j+\frac{1}{2},k+\frac{1}{2}} = E^x\big(z_i, x_{j+\frac{1}{2}}, y_{k+\frac{1}{2}}\big),$$
$$E^y_{i,j,k} = E^y(z_i, x_j, y_k)$$

for the electric field components, while the magnetic field components are collocated as

$$H^z_{i,j+\frac{1}{2},k} = H^z\big(z_i, x_{j+\frac{1}{2}}, y_k\big), \quad H^x_{i+\frac{1}{2},j,k} = H^x\big(z_{i+\frac{1}{2}}, x_j, y_k\big),$$
$$H^y_{i+\frac{1}{2},j+\frac{1}{2},k+\frac{1}{2}} = H^y\big(z_{i+\frac{1}{2}}, x_{j+\frac{1}{2}}, y_{k+\frac{1}{2}}\big).$$

Following the notation in Section 3.1.1 we have introduced the staggered grids

$$z_i = h_z i, \quad z_{i+\frac{1}{2}} = h_z\left(i + \frac{1}{2}\right),$$

and likewise for the nodes in x and y.

To appreciate the generalization of the two-dimensional treatment of curved interfaces to the three-dimensional case, let us, as an example, consider a situation as depicted in Fig. 7. Here a surface intersects the z-axis, forcing one to consider a special scheme for updating E^y, as the z-derivative of H^x is required. The interface conditions, shown in Eq. (53), yield the explicit relation between the magnetic field components on either side of the interface. However, these conditions have six unknowns but supply only four conditions. Moreover, because of the structure of the conditions, only three of the conditions are linearly independent, i.e., we shall need to recover three of the field components from the grid solution by extrapolation.

Similar to the two-dimensional case, one recovers $H^{x,(1)}$ directly by extrapolation

$$H^{x,(1)} = \big(1 + \gamma^{(1)}_{i,j,k}\big) H^x_{i-\frac{1}{2},j,k} - \gamma^{(1)}_{i,j,k} H^x_{i-\frac{3}{2},j,k},$$

where $\gamma^{(1)}_{i,j,k} = \frac{1}{2} - \gamma^{(2)}_{i,j,k}$ assuming a generalization of the notation in Fig. 7. For the special case where $\hat{n}_x = 0$, this is sufficient as H^x is tangential to the interface and one recovers

$H^{x,(2)}$ directly through continuity. For the general case, one recovers an approximation to $H^{x,(2)}$ using

$$\tilde{H}^z_{j\pm\frac{1}{2},k} = \left(1+\gamma^{(2)}_{i,j\pm\frac{1}{2},k}\right)H^z_{i,j\pm\frac{1}{2},k} - \gamma^{(2)}_{i,j\pm\frac{1}{2},k}H^z_{i+1,j\pm\frac{1}{2},k},$$

and approximating $H^{z,(2)}$ as

$$H^{z,(2)} = \frac{\tilde{H}^z_{j+\frac{1}{2},k} + \tilde{H}^z_{j-\frac{1}{2},k}}{2},$$

as in the two-dimensional case.

Maintaining the basic approach that extrapolations do not extend beyond half a grid cell, we are left only with the option of estimating $H^{y,(1)}$. Since

$$H^y_{i+\frac{1}{2},j+\frac{1}{2},k+\frac{1}{2}}$$

is sitting in plane with

$$H^x_{i+\frac{1}{2},j,k}$$

but out of plane with $E^y_{i,j,k}$, we may construct an approximation to $H^{y,(1)}$ through the introduction of four variables which are found though extrapolation along the z-axis as

$$\tilde{H}^y_{j\pm\frac{1}{2},k\pm\frac{1}{2}} = \left(1+\gamma^{(1)}_{i,j\pm\frac{1}{2},k\pm\frac{1}{2}}\right)H^y_{i-\frac{1}{2},j\pm\frac{1}{2},k\pm\frac{1}{2}} - \gamma^{(1)}_{i,j\pm\frac{1}{2},k\pm\frac{1}{2}}H^y_{i-\frac{3}{2},j\pm\frac{1}{2},k\pm\frac{1}{2}},$$

where

$$\gamma^{(2)}_{i,j\pm\frac{1}{2},k\pm\frac{1}{2}} = \frac{1}{2} - \gamma^{(1)}_{i,j\pm\frac{1}{2},k\pm\frac{1}{2}}$$

is a relative measure of the distance between the i-grid plane and the interface measured along the z-axis, i.e., it is a straightforward generalization of the extrapolation utilized for $H^{z,(2)}$ in the two-dimensional situation depicted in Fig. 7.

From these extrapolated values, $H^{y,(1)}$ is approximated as

$$H^{y,(1)} = \frac{1}{4}\left(\tilde{H}^y_{j-\frac{1}{2},k-\frac{1}{2}} + \tilde{H}^y_{j+\frac{1}{2},k-\frac{1}{2}} + \tilde{H}^y_{j+\frac{1}{2},k+\frac{1}{2}} + \tilde{H}^y_{j-\frac{1}{2},k+\frac{1}{2}}\right),$$

and the unknown $H^{x,(2)}$, required to update E^y, is then recovered by enforcing the boundary conditions to obtain

$$H^{x,(2)} = H^{x,(1)} + \hat{n}_x\left(\mu^{(1)}-\mu^{(2)}\right)\frac{\hat{n}_z H^{z,(2)} + \hat{n}_x H^{x,(1)} + \hat{n}_y H^{y,(1)}}{\mu^{(1)}\hat{n}_z^2 + \mu^{(2)}\hat{n}_x^2 + \mu^{(2)}\hat{n}_y^2}.$$

We note in particular that for $\hat{n}_x = 0$ one recovers continuity as expected and for $\hat{n}_y = 0$ one obtains the expression derived for the two-dimensional situation.

Clearly, to update the remaining two electric field components an equivalent procedure can be used when the grid point sits close to a material interface. Moreover, to update

magnetic field components positioned next to an interface one can simply exploit the duality of Maxwell's equations and exchange the magnetic interface conditions with the ones governing the electric fields to obtain expressions equivalent to the above.

Let us briefly consider a situation in which the interface is perfectly conducting. In this case the boundary conditions take the form

$$\boldsymbol{n} \times \boldsymbol{E} = 0, \quad \boldsymbol{n} \cdot \boldsymbol{H} = 0,$$

i.e., there are two linearly independent conditions on $\boldsymbol{E}$ while only one condition on $\boldsymbol{H}$ exists. The equivalent Neumann conditions are obtained by combining these Dirichlet conditions with the equations themselves.

Considering a situation as in Fig. 7, we can exploit that E^x and E^y are located in the same plane of the staggered grid such that by computing

$$\tilde{E}^x_{j\pm\frac{1}{2},k\pm\frac{1}{2}} = \left(1 + \gamma^{(2)}_{i,j\pm\frac{1}{2},k\pm\frac{1}{2}}\right) E^x_{i,j\pm\frac{1}{2},k\pm\frac{1}{2}} - \gamma^{(2)}_{i,j\pm\frac{1}{2},k\pm\frac{1}{2}} E^x_{i-1,j\pm\frac{1}{2},k\pm\frac{1}{2}},$$

with

$$\gamma^{(2)}_{i,j\pm\frac{1}{2},k\pm\frac{1}{2}}$$

being a relative measure of the distance between the i-grid plane and the interface measured along the z-axis, one can approximate $E^{x,(2)}$ at the conductor as

$$E^{x,(2)} = \frac{1}{4}\left(\tilde{E}^x_{j-\frac{1}{2},k-\frac{1}{2}} + \tilde{E}^x_{j+\frac{1}{2},k-\frac{1}{2}} + \tilde{E}^x_{j+\frac{1}{2},k+\frac{1}{2}} + \tilde{E}^x_{j-\frac{1}{2},k+\frac{1}{2}}\right),$$

and, hence, obtain an approximation to $E^{y,(2)}$ through the boundary conditions as

$$E^{y,(2)} = \frac{\hat{n}_y}{\hat{n}_x} E^{x,(2)},$$

provided only $\hat{n}_x \neq 0$. With this, we can then simply update $E^y_{i,j,k}$ as

$$E^y_{i,j,k} = \frac{1}{1 + \gamma^{(2)}_{i,j,k}} \left(\gamma^{(2)}_{i,j,k} E^y_{i+1,j,k} + E^{y,(2)}\right).$$

In the very special case of $\hat{n}_x = 0$ one can complete the scheme by using the Neumann conditions on the magnetic field components similar to the one-dimensional case. We shall not give the details here as it represents only one of many special cases that will need attention in an actual implementation but are dealt with using the same basic ideas outlined in the above.

3.2. A Note on the Implementation

The various schemes presented in the above all utilize extrapolations and one-sided stencils that depend on the position of the intersecting interface/boundary close to each individual grid point. Indeed, it may seem as if the accuracy of the general scheme is

achieved at the expense of computational inefficiency and becomes complex because of the large variability of schemes used in different places of the grid.

The situation is, however, not so bleak provided a few simple observations are utilized. The computation of the subgrid parameters, $\gamma_{i,j,k}$, specifying the exact position of the material interfaces and the metallic boundaries, can naturally be done in a preprocessing stage as can the computation of the normal vectors of the surfaces intersecting the grid axis.

The schemes, combining extrapolation and one-sided differences, can be recast as non-central difference schemes with a special scheme for each point close to the interfaces, i.e., if we consider the one-dimensional scheme discussed in detail in Section 2.1 it takes the form

$$\mu^{(1)}\frac{dH^{(1)}_{N-\frac{1}{2}}}{dt} = \frac{1}{\left(2\gamma_R^{(1)}+1\right)h}\left[\left(2\gamma_R^{(1)}+1\right)E_1^{(2)} + \left(3-2\gamma_R^{(1)}\right)E_0^{(2)} - 2E^{(1)}_{N-1}\right],$$

for updating $H^{(1)}_{N-\frac{1}{2}}$ while we recover

$$\varepsilon^{(2)}\frac{dE_0^{(2)}}{dt} = \frac{1}{\left(2\gamma_R^{(2)}+1\right)h}\left[2H^{(2)}_{\frac{1}{2}} - \left(3-2\gamma_L^{(1)}\right)H^{(1)}_{N-\frac{1}{2}} - \left(2\gamma_L^{(1)}-1\right)H^{(1)}_{N-\frac{3}{2}}\right],$$

for updating $E_0^{(2)}$.

For the multidimensional schemes, a very similar construction can be utilized. The main difference is, however, that the stencils in general become multidimensional close to the boundaries because of the need for additional information to correctly enforce the boundary conditions. However, as this is all constructed in a preprocessing stage it does not affect the overall computational requirements of the scheme in a significant manner.

An appealing alternative implementation is that of a predictor–corrector scheme in which an existing Yee scheme, serving as the predictor stage, is used to evaluate Maxwell's equations everywhere while a corrector stage modifies the solutions locally according to the proposed scheme. This approach has the advantage that it can be built directly on top of existing finite-difference time-domain production codes, yielding a dramatic improvement in accuracy at little computational expense beyond the preprocessing stage, where the corrector step is initialized. Only additional storage for the special stencils required to update the points close to the interfaces is needed.

3.3. Accuracy Revisited

To appreciate the particular importance of correctly imposing the jump-conditions when solving multidimensional problems, and the consequences of not doing so in the Yee scheme, we shall consider an illustrative example.

We consider the TE form of the two-dimensional Maxwell's equations

$$\begin{aligned}
\varepsilon\frac{\partial E^z}{\partial t} &= \frac{\partial H^y}{\partial x}\\
\varepsilon\frac{\partial E^x}{\partial t} &= -\frac{\partial H^y}{\partial z},\\
\mu\frac{\partial H^y}{\partial t} &= \frac{\partial E^z}{\partial x} - \frac{\partial E^x}{\partial z},
\end{aligned} \tag{54}$$

and we recall that the boundary conditions between two regions, with the material parameters, $\varepsilon^{(k)}$ and $\mu^{(k)}$, and the fields, $(E^{z,(k)}, E^{x,(k)}, H^{y,(k)})$ for $k = 1, 2$, take the form

$$\hat{\boldsymbol{n}} \times \boldsymbol{E}^{(1)} = \hat{\boldsymbol{n}} \times \boldsymbol{E}^{(2)}, \tag{55}$$

$$\varepsilon^{(1)} \hat{\boldsymbol{n}} \cdot \boldsymbol{E}^{(1)} = \varepsilon^{(2)} \hat{\boldsymbol{n}} \cdot \boldsymbol{E}^{(2)}, \tag{56}$$

$$H^{y,(1)} = H^{y,(2)}, \tag{57}$$

where $\boldsymbol{E}^{(k)} = (E^{z,(k)}, E^{x,(k)}, 0)^T$ and $\hat{\boldsymbol{n}} = (\hat{n}_z, \hat{n}_x, 0)^T$ represents a unit vector normal to the interface.

Let us assume that the physical situation is as illustrated in Fig. 7, with the difference that the TE form rather than the TM form is being solved, i.e., the unknown variables are collocated as

$$E^z_{i,j+\frac{1}{2}} = E^z\big(z_i, x_{j+\frac{1}{2}}\big), \quad E^x_{i+\frac{1}{2},j} = E^x\big(z_{i+\frac{1}{2}}, x_j\big), \quad H^y_{i,j} = H^y(z_i, x_j).$$

Since H^y is tangential to the material interface, it is continuous across the interface and we can take $\mu^{(1)} = \mu^{(2)} = 1$. Without loss of generality we can also take $\varepsilon^{(1)} = 1$.

We consider a situation in which a plane wave impinges on the interface from the left propagating along the z-axis. Since $\varepsilon^{(1)} = 1$ we have that $E^{z,(1)} = 0$ while the remaining field components are related as

$$\hat{n}_z E^{x,(1)} = \hat{n}_z E^{x,(2)} - \hat{n}_x E^{z,(2)},$$
$$\hat{n}_x E^{x,(1)} = \varepsilon\big(\hat{n}_x E^{x,(2)} + \hat{n}_z E^{z,(2)}\big),$$

using Eqs. (55) and (56) and taking $\varepsilon = \varepsilon^{(2)}$ for simplicity. If we now eliminate $E^{z,(2)}$ we recover a relation such as

$$E^{x,(1)} = \frac{\varepsilon}{\varepsilon \hat{n}_z^2 + \hat{n}_x^2} E^{x,(2)} = \frac{\varepsilon}{1 + (\varepsilon - 1)\cos^2\theta} E^{x,(2)}, \tag{58}$$

where θ simply represents the angle between $\hat{\boldsymbol{n}}$ and the z-axis. We observe that for $\theta = 0$, E^x is continuous as expected, while for $\theta = \pi/2$ it experiences a maximum jump as it becomes a purely normal component. The degree of discontinuity of E^x across the interface in controlled solely by ε and θ.

This result suggests that we can in fact model the implications of having a two-dimensional problem with a general curved material interface by simply considering the one-dimensional situation discussed in depth in Section 2.4, however modified such that the condition on E^x across the interface is given by Eq. (58).

The exact solution to this problem is easily recovered from Eqs. (33) and (34) with $n^{(1)} = 1, n^{(2)} = \sqrt{\varepsilon}$, and the only difference being that ω is obtained as the solution to the equation

$$\tan\omega = \frac{-\sqrt{\varepsilon}\tan(\sqrt{\varepsilon}\omega)}{1 + (\varepsilon - 1)\cos^2\theta}.$$

As a simple test case, we shall take $\varepsilon = 2.25$ for which the exact solution at $t = 0$ is given in Fig. 8 for the case of $\theta = 30°$. As expected, we see a small jump in the E^x component as a consequence of the interface not being aligned with the grid.

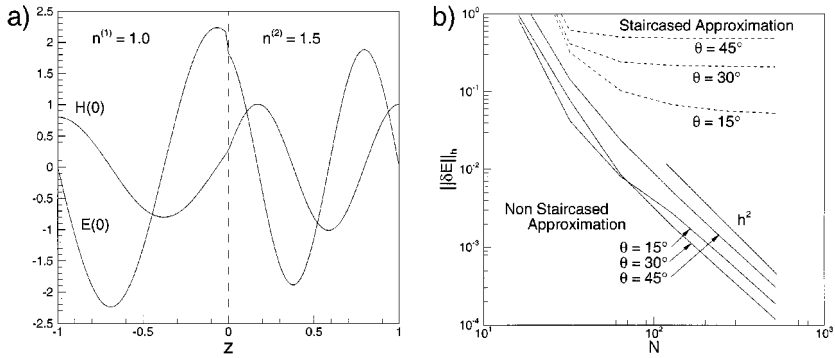

FIG. 8. In a) we illustrate the initial conditions for the modified one-dimensional cavity problem in the case where the material interface is assumed tilted at $\theta = 30°$. In b) we show the global L^2-error of E for different angles, i.e., the degree of discontinuity of E at the interface, as computed using the staggered Yee scheme and the new non-staggered approximation.

We shall now attempt to model this problem using the Yee scheme and the newly developed scheme. The computational setup is exactly as in Section 2.4 and to make things even simpler we assume that $\gamma = 0$, i.e., the material interface is located at a grid point although the interface generally is tilted at some angle.

Because of the nature of the Yee scheme, it is unable to correctly model the discontinuous field component which the scheme simply assumes to be smooth, i.e., an essential characteristic of the field behavior is removed. As shown in Fig. 8, a consequence of this is that the Yee scheme is globally nonconvergent for a problem with a discontinuous solution, as was predicted in the analysis in Section 2.4. A manifestation of the very badly approximated discontinuous solution is the introduction of a spurious DC component with a magnitude that is directly proportional to the size of the jump, as shown in Eq. (35). Careful inspection of the computational results in Fig. 8 confirms this. One should recall that while one observes global nonconvergent behavior, the solution is locally divergent.

Using the new method, however, the correct solution is recovered to global second-order accuracy, yielding a fidelity that is orders of magnitude better than obtained with the Yee scheme with comparable computational work.

The relevance of this study is two-fold. On one hand it demonstrates the ability of the new scheme to accurately and efficiently model problems with discontinuous solutions. Secondly, and perhaps most importantly, it illustrates the inability of the Yee scheme to handle such problems.

The use of staircasing at a material interface completely removes the discontinuity of the individual field components with the exception of the normal component. However, because only derivatives of tangential components are required, this does not pose a problem. On the other hand, an essential property of the almost tangential components, in the above case E^x, has been lost by introducing the staircasing. As we have seen in the above, the impact of this is that the Yee scheme may become nonconvergent for very general classes of problems.

3.4. Further Numerical Tests

To further illustrate the performance of the new scheme for more general multidimensional problems we consider in the following the solution of two different problems which

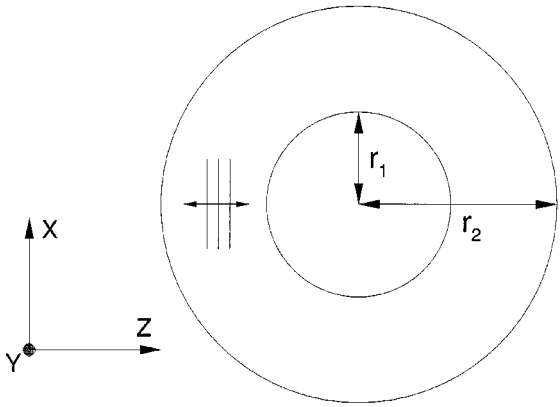

FIG. 9. Illustration of the perfectly conducting annular circular cylinder and the geometry of the computational test.

are simple enough that exact solutions exist, yet complex enough not to be trivial. Similar to the one-dimensional cases, the solutions are advanced in time using a fourth-order Runge–Kutta method. As a point of reference we shall compare with results obtained using the Yee scheme, albeit with Runge–Kutta time-stepping rather than Leapfrog. This, however, has no implications for the validity of the conclusions.

We shall focus the attention on solving the two-dimensional TM form of Maxwell's equations for (H^z, H^x, E^y) on the form

$$\begin{aligned}
\mu \frac{\partial H^z}{\partial t} &= -\frac{\partial E^y}{\partial x}, \\
\mu \frac{\partial H^x}{\partial t} &= \frac{\partial E^y}{\partial z}, \\
\varepsilon \frac{\partial E^y}{\partial t} &= \frac{\partial H^x}{\partial z} - \frac{\partial H^z}{\partial x}.
\end{aligned}$$

As our first case, testing the effects of staircasing only, we shall consider the modeling of a PEC resonator as shown in Fig. 9. It consists of two concentric PEC cylinders with an electromagnetic wave trapped between the walls. The material is taken to be vacuum, i.e., $\varepsilon = \mu = 1$ in normalized units.

As discussed in Section 3.1.1, the boundary condition at the wall is simply that $E^y = 0$, leading to an exact time-domain solution for a cylindrical wave as

$$\begin{aligned}
H^z(z, x, t) = &-\frac{1}{2} \sin(\omega t + \theta) \sin\theta [J_0(\omega r) - J_2(\omega r) + a(Y_0(\omega r) - Y_2(\omega r))] \\
&- \frac{\cos\theta}{\omega r} \cos(\omega t + \theta)[J_1(\omega r) + aY_1(\omega r)],
\end{aligned}$$

$$\begin{aligned}
H^x(z, x, t) = &\frac{1}{2} \sin(\omega t + \theta) \cos\theta [J_0(\omega r) - J_2(\omega r) + a(Y_0(\omega r) - Y_2(\omega r))] \\
&- \frac{\sin\theta}{\omega r} \cos(\omega t + \theta)[J_1(\omega r) + aY_1(\omega r)],
\end{aligned}$$

$$E^y(z, x, t) = \cos(\omega t + \theta)[J_1(\omega r) + aY_1(\omega r)],$$

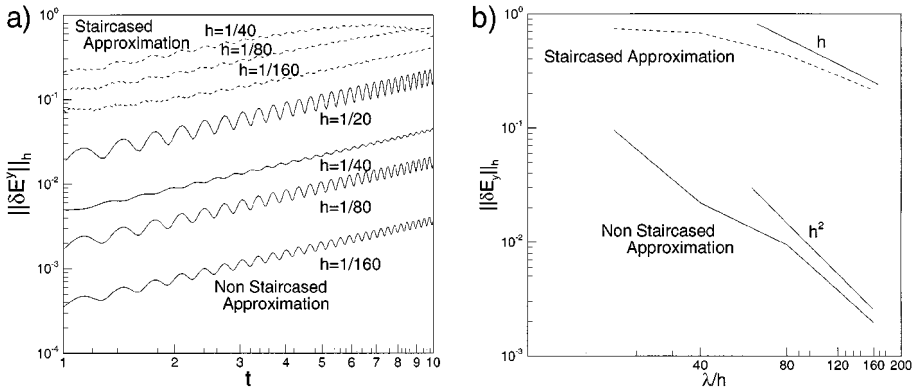

FIG. 10. In a) we show the temporal dependence of the global L^2 error of E^y for different resolution in terms of the free-space wavelength for the staircased and non-staircased approximation. In b) is shown the global error at t = 5, clearly illustrating the expected convergence rate.

where $(r, \theta) = (\sqrt{z^2 + x^2}, \arctan \frac{x}{z})$ represent the usual polar coordinates, and J_n and Y_n signify the n-th order Bessel functions of the first and second kind, respectively.

The constants, ω and a, are obtained by enforcing the boundary conditions on E^y at $r = r_1$ and $r = r_2$, respectively. In this particular case, we shall take $r_1 = \frac{1}{6}$ and $r_2 = \frac{1}{2}$, implying that $\omega \simeq 9.813695999428405..$ and $a \simeq 1.76368380110927..$

In Fig. 10 we show the results of the simulations using the Yee scheme as well as the new scheme where no staircasing of the boundary is introduced. Using as little as 20 points per wavelength, but accounting for the boundary correctly, yields close to an order of magnitude better result as compared to the Yee scheme with 160 points per wavelength. If we recall the two-dimensional nature of the problem this implies an $8^2 = 64$-fold reduction of the degrees of freedom, and hence an $8^3 = 512$-fold reduction in computing time, while improving the accuracy. The global second-order convergence of the nonstaircased approximation is also illustrated in Fig. 10, which furthermore confirms that only first-order convergence can be expected for the Yee scheme as observed in the one-dimensional tests in Section 2.4.

As an example of a problem with a material interface, let us consider the scenario shown in Fig. 11 in which a plane wave impinges on a di-electric cylinder, experiencing reflection and refraction at the material interface. The problem is solved in a scattered field/total

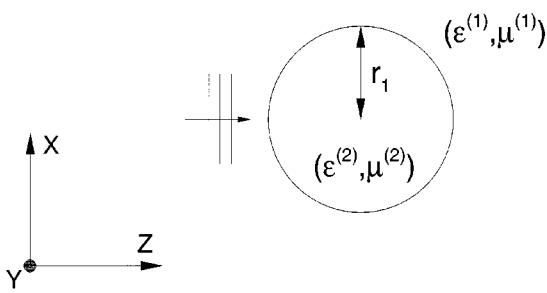

FIG. 11. Illustration of the general di-electric cylinder, $r_1 = \frac{\pi}{12}$ and $\varepsilon^{(2)} = 12.96$ and the geometry of the computational test.

field formulation [7], and a stabilized PML method [4] is used to terminate the rectangular computational domain.

We shall consider a situation in which $\mu^{(1)} = \mu^{(2)} = \varepsilon^{(1)} = 1$, i.e., the material is non-magnetics, and the material exterior to the cylinder is assumed to be vacuum. The cylinder is assumed to have a radius of $r_1 = \frac{\pi}{12}$ and index of refraction of $\sqrt{\varepsilon^{(2)}} = 3.6$. As discussed in Section 3.1.1, this implies that each of the three field components are continuous across the material interface and the one-dimensional scheme can be used directly to enforce the material boundary conditions. In terms of accuracy, this case is the one best suited for the Yee scheme. As we shall see shortly, however, its performance is very far from satisfactory even for this case.

If we assume that the cylinder is illuminated by a plane monochromatic unit wavelength wave of the form

$$E^y_{\text{inc}} = \exp(-i2\pi(z-\omega t)), \quad H^x_{\text{inc}} = -\exp(-i2\pi(z-\omega t)),$$

the exact solution to the scattering problem is given as

$$E^y(z,x,t) = \exp(i2\pi\omega t)\begin{cases} \sum_{n=-\infty}^{\infty} C_n^{\text{tot}} J_n(2\pi\sqrt{\varepsilon}r)\exp(-in\theta) & r \le r_1 \\ \exp(i2\pi z) + \sum_{n=-\infty}^{\infty} C_n^{\text{scat}} H_n^{(2)}(2\pi r)\exp(-in\theta) & r \ge r_1 \end{cases},$$

where J_n and $H_n^{(2)}$ represents the n-th order Bessel function of the first kind and the Hankel function of the second kind, respectively, while $\varepsilon = \varepsilon^{(2)}$ for simplicity. As in the first test case, $(r,\theta) = (\sqrt{z^2+x^2}, \arctan\frac{x}{z})$ represents the usual polar coordinates.

The expansion coefficients for the total field interior to the cylinder are given as

$$C_n^{\text{tot}} = (-i)^n \frac{\chi_1^J H_n^{(2)}(2\pi r_1) - \chi_1^{H^{(2)}} J_n(2\pi r_1)}{\sqrt{\varepsilon}\chi_2^J H_n^{(2)}(2\pi\sqrt{\varepsilon}r_1) - \chi_1^{H^{(2)}} J_n(2\pi\sqrt{\varepsilon}r_1)},$$

with

$$\chi_1^V = V_{n-1}(2\pi r_1) - V_{n+1}(2\pi r_1), \quad \chi_2^V = V_{n-1}(2\pi\sqrt{\varepsilon}r_1) - V_{n+1}(2\pi\sqrt{\varepsilon}r_1),$$

where V may represent J and $H^{(2)}$. The corresponding coefficients for the scattered field are given as

$$C_n^{\text{scat}} = \frac{C_n^{\text{tot}} J_n(2\pi\sqrt{\varepsilon}r_1) - (-i)^n J_n(2\pi r_1)}{H_n^{(2)}(2\pi r_1)}.$$

Using Maxwell's equations, one can then recover the solutions for the magnetic field components.

Similar to the previous case, we show in Fig. 12 the temporal behavior of the global error as well as the result of a resolution study at a specific time. As for the pure metallic case we see that incorrect treatment of boundaries and their position severely limits the accuracy of the Yee scheme which remains first-order accurate. Unfortunately, this is only what one should expect based on the analysis presented earlier. Contrary to this, the new scheme is truly second order and typically yields at least an order of magnitude improvement in

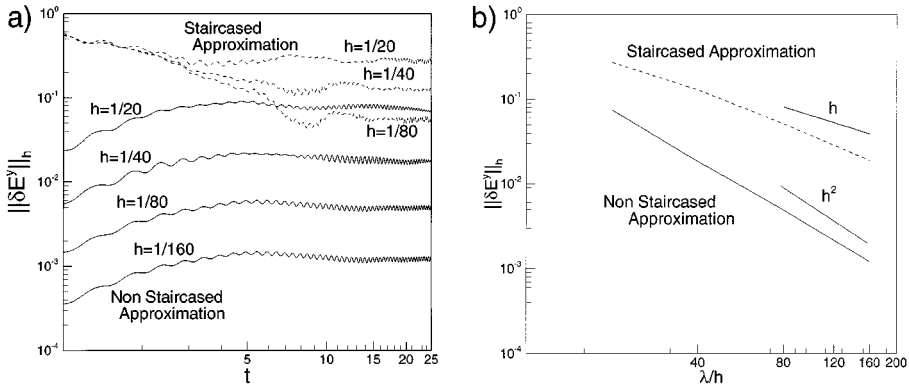

FIG. 12. In a) we show the temporal dependence of the global L^2 error of E^y for different resolution in terms of the free-space wavelength for the staircased and non staircased approximation. In b) is shown the global error at $t = 25$, illustrating the expected convergence rate.

accuracy over the Yee scheme for the same resolution and, thus, the same work. Moreover, one should keep in mind that these results are obtained for a test case for which the Yee scheme is particularly well suited, as all field components are continuous. As we have illustrated in the previous section, the situation can be expected to be much worse for problems with discontinuous field components, which, after all, is the norm rather than the exception.

4. FINAL REMARKS

The purpose of this paper has been two-fold. On one hand, we presented a detailed accuracy analysis of the Yee scheme, which continues to be the main workhorse of time-domain computational electromagnetics. As is well known, and confirmed through the analysis and the computational examples presented, the need in the Yee scheme to introduce a staircased approximation of curved metallic boundaries dramatically reduces the overall accuracy of the scheme which at best is first-order in such cases. However, the situation at transparent interfaces is even more troubling. Because the Yee scheme is applied everywhere in the computational domain, no effort is made to impose the proper jump conditions on the electric and magnetic fields. Since these are continuous at best, this clearly introduces another source of significant error which has received limited attention in the literature. Indeed, as we have argued through analysis and confirmed through a very simple computational example, the combination of staircasing and the lack of imposing the proper jump-conditions may well result in a nonconvergent approximation. This is a result of the elimination of almost tangential discontinuous field components, i.e., a fundamental physical property has been removed. No averaging of material properties or a variety of other simple techniques can restore this property.

It has been the purpose of the second topic of this paper to present a novel second-order scheme, building on the superior behavior of the Yee scheme in homogeneous regions and utilizing the same spatially staggered grid, yet modified in such a way that the need for staircasing is eliminated and physical jump-conditions are imposed to the order of the scheme. The scheme is globally second-order accurate for arbitrarily embedded interfaces,

and we have shown it to be convergent by proving it to be a bounded error scheme. Moreover, the main source of complication as compared to the Yee scheme lies in a preprocessing phase where the location of the embedded interfaces is determined and where specialized stencils are constructed. After that, the overall work is essentially identical to that of the Yee scheme with a similar CFL restriction for discrete stability. However, for comparable resolution, this new scheme typically yields one to two orders of magnitude improvement in the accuracy as has been illustrated through one- and two-dimensional test cases.

While the proposed scheme offers a fairly straightforward way of improving existing Yee-based computational engines and eliminates the two most severe sources of errors, it does not change the fact that using high-order schemes for solving the time-domain equations almost certainly is needed to facilitate the accurate and efficient solution of large time-dependent problems. By directly extending the ideas introduced in this paper, the first steps in the development of suitable fourth-order schemes have been taken in [25], where a one-dimensional fourth-order scheme has been studied computationally, yielding very promising results. Encouraged by these results and by our own initial studies, we hope to present a stable fourth-order accurate Cartesian grid method for Maxwell's equations in the near future.

APPENDIX: PROOF OF BOUNDED ERROR PROPERTY

In Section 2.3 we sketched the proof of bounded error behavior for the proposed scheme without providing a number of details of the constructive proof. It is the purpose of this appendix to rectify this neglect.

We shall continue the use of the notation introduced in Section 2.3 and recall that the bounded error property is closely linked to the properties of the matrix operator, M, given in Eq. (25), which describes the propagation of the error as

$$\frac{d\boldsymbol{\epsilon}}{dt} = M\boldsymbol{\epsilon} + \boldsymbol{T}.$$

Here $\boldsymbol{\epsilon} = \boldsymbol{u} - \boldsymbol{v}$, where $\boldsymbol{u}$ represents the projection of the exact solution on the grid, $\boldsymbol{v}$ is the numerical solution, and $\boldsymbol{T}$ represents a grid vector of the local pointwise truncation error.

Following the notation of Eq. (25), the three submatrices of M are given as

$$\mathrm{M}^L = \begin{bmatrix} 0 & -\frac{\gamma_L^{(1)}}{1+\gamma_L^{(1)}}c^{(1)} & 0 & \frac{\gamma_L^{(1)}}{1+\gamma_L^{(1)}}c^{(1)} & & & \\ 0 & 0 & \frac{1}{1+\gamma_L^{(1)}}c^{(1)} & 0 & & & \\ 0 & -c^{(1)} & 0 & c^{(1)} & & & \\ 0 & 0 & -c^{(1)} & 0 & c^{(1)} & & \\ & & & \ddots & \ddots & \ddots & \\ & & & & -c^{(1)} & 0 & c^{(1)} \\ & & & & & -c^{(1)} & 0 \end{bmatrix}, \tag{A.1}$$

$$
\mathrm{M}^{M} = \begin{bmatrix}
0 & c^{(1)} & & & & & & & & & & \\
-c^{(1)} & 0 & c^{(1)} & & & & & & & & & \\
 & \ddots & \ddots & \ddots & & & & & & & & \\
 & & -c^{(1)} & 0 & c^{(1)} & 0 & 0 & 0 & & & & \\
 & & & -c^{(1)} & 0 & c^{(1)} & 0 & 0 & & & & \\
 & & & 0 & \frac{-2c^{(1)}}{1+2\gamma_R^{(1)}} & 0 & \frac{3-2\gamma_R^{(1)}}{1+2\gamma_R^{(1)}}\frac{c^{(2)^2}}{c^{(1)}} & 0 & -\frac{1-2\gamma_R^{(1)}}{1+2\gamma_R^{(1)}}\frac{c^{(2)^2}}{c^{(1)}} & & & \\
 & & & \frac{\gamma_R^{(1)}c^{(1)}}{1-\gamma_R^{(1)}} & 0 & -\frac{1+\gamma_R^{(1)}}{1-\gamma_R^{(1)}}c^{(1)} & 0 & \frac{c^{(2)}}{1-\gamma_R^{(1)}} & 0 & & & \\
 & & & 0 & 0 & 0 & -c^{(2)} & 0 & c^{(2)} & & & \\
 & & & 0 & 0 & 0 & 0 & -c^{(2)} & 0 & c^{(2)} & & \\
 & & & & & & & & \ddots & \ddots & \ddots & \\
 & & & & & & & & & -c^{(2)} & 0 & c^{(2)} \\
 & & & & & & & & & & -c^{(2)} & 0
\end{bmatrix}, \qquad \text{(A.2)}
$$

and

$$\mathrm{M}^R = \begin{bmatrix} 0 & c^{(2)} & & & & & \\ -c^{(2)} & 0 & c^{(2)} & & & & \\ & \ddots & \ddots & \ddots & & & \\ & & 0 & -c^{(2)} & 0 & c^{(2)} & \\ & & & 0 & -\frac{2}{1+2\gamma_R^{(2)}}c^{(2)} & 0 & \end{bmatrix}. \tag{A.3}$$

Note that in M^M, near the material interface, we used only $\gamma_R^{(1)}$ by exploiting the fact that $\gamma_R^{(1)} + \gamma_R^{(2)} = \frac{1}{2}$.

With this in place, we shall now need to establish that M is similar to an antisymmetric matrix for all values of h, $\gamma_L^{(k)}$, and $\gamma_R^{(k)}$. The first step is to rewrite M as

$$\mathrm{M} = \mathrm{Q}^{-1}\mathrm{A}\mathrm{Q},$$

where A is an antisymmetric matrix. That this can be done is by no means obvious, and we can only present a constructive proof.

The structure of A is given in Eq. (27) and we postulate that the submatrix A^L takes the form

$$\mathrm{A}^L = \begin{bmatrix} 0 & 0 & 0 & 0 & & & \\ 0 & 0 & \sqrt{\frac{1}{1+\gamma_L^{(1)}}}c^{(1)} & & & & \\ 0 & -\sqrt{\frac{1}{1+\gamma_L^{(1)}}}c^{(1)} & 0 & c^{(1)} & & & \\ 0 & 0 & -c^{(1)} & 0 & c^{(1)} & & \\ & & & \ddots & \ddots & \ddots & \\ & & & & -c^{(1)} & 0 & c^{(1)} \\ & & & & & -c^{(1)} & 0 \end{bmatrix}, \tag{A.4}$$

while the lower right submatrix A^R shall be given as

$$\mathrm{A}^R = \begin{bmatrix} 0 & c^{(1)} & & & & \\ -c^{(1)} & 0 & c^{(1)} & & & \\ & \ddots & \ddots & \ddots & & \\ & & 0 & -c^{(1)} & 0 & \sqrt{\frac{2}{1+2\gamma_R^{(2)}}}c^{(2)} \\ & & & 0 & -\sqrt{\frac{2}{1+2\gamma_R^{(2)}}}c^{(2)} & 0 \end{bmatrix}. \tag{A.5}$$

The final central matrix A^M takes the form

$$\mathrm{A}^M = \begin{bmatrix}
0 & c^{(1)} & & & & & & & & & & & & \\
-c^{(1)} & 0 & c^{(1)} & & & & & & & & & & & \\
 & \ddots & \ddots & \ddots & & & & & & & & & & \\
 & & -c^{(1)} & 0 & c^{(1)} & & & & & & & & & \\
 & & & -c^{(1)} & 0 & c^{(1)} & 0 & 0 & 0 & 0 & & & & \\
 & & & & -c^{(1)} & 0 & a_1 & a_4 & a_5 & 0 & & & & \\
 & & & & 0 & -a_1 & 0 & a_2 & 0 & 0 & & & & \\
 & & & & 0 & -a_4 & -a_2 & 0 & a_3 & 0 & & & & \\
 & & & & 0 & -a_5 & 0 & -a_3 & 0 & c^{(2)} & & & & \\
 & & & & 0 & 0 & 0 & 0 & -c^{(2)} & 0 & c^{(2)} & & & \\
 & & & & & & & & & -c^{(2)} & 0 & c^{(2)} & & \\
 & & & & & & & & & & \ddots & \ddots & \ddots & \\
 & & & & & & & & & & & -c^{(2)} & 0 & c^{(2)} \\
 & & & & & & & & & & & & -c^{(2)} & 0
\end{bmatrix}, \tag{A.6}$$

where the entries are given as

$$a_1 = c^{(1)} - \frac{\sqrt{\gamma_R^{(1)} - 2\gamma_R^{(1)^2}}}{\sqrt{1 + \gamma_R^{(1)} - 2\gamma_R^{(1)^2}}} c^{(2)}, \quad a_2 = a_3 = \frac{2c^{(2)}}{\sqrt{2 + 2\gamma_R^{(1)} - 4\gamma_R^{(1)^2}}} c^{(2)},$$

$$a_4 = \frac{\sqrt{1 - 3\gamma_R^{(1)} + 2\gamma_R^{(1)^2}}\, c^{(1)} - \sqrt{\gamma_R^{(1)} + 2\gamma_R^{(1)^2}}\, c^{(2)}}{\sqrt{1 + \gamma_R^{(1)} - 2\gamma_R^{(1)^2}}}, \quad a_5 = \frac{\sqrt{\gamma_R^{(1)} - 2\gamma_R^{(1)^2}}\, c^{(2)}}{\sqrt{1 + \gamma_R^{(1)} - 2\gamma_R^{(1)^2}}}.$$

To fix the notation, note that M^L as well as A^L has a 4×4 block in its upper-left corner and a tri-diagonal Toeplitz tail. We shall denote M^L of rank $n+4$ as M_n^L, its determinant by d_n^L, and its characteristic polynomial by p_n^L. In a similar fashion, we note that M^R and A^R both have a 2×2 block in their lower right corner and a tri-diagonal Toeplitz head. Thus for M^R of rank $n+2$ we use the analog M_n^R, d_n^R, and p_n^R notations. Finally, M^M and A^M have both a 6×6 central block and a tri-diagonal "head" and "tail." For this more general case, we shall use the notation $\mathrm{M}_{m,n}^M$, $\mathrm{d}_{m,n}^M$, $\mathrm{p}_{m,n}^M$ to signify M^M with head length of m and tail length of n and the corresponding determinant and characteristic polynomial. An equivalent notation shall be used to refer to the submatrices of A, their determinants, and their characteristic polynomials.

To establish that A and M share the same characteristic polynomial, we shall need the following Lemma.

LEMMA A.1. *Let Q_{n-1}^L be a rank $(n-1)$ matrix with the following structure*

$$Q_{n-1}^L = \begin{bmatrix}
B_k & & \\
 & \lfloor & c \\
 & a & b \quad c \\
 & & a \quad b
\end{bmatrix},$$

where B_k is an $k \times k$ matrix block. Clearly, $k < n-1$. Assume that Q_n^L and Q_{n+1}^L be matrices with a similar structure, and let d_{n-1}^L, d_n^L, and d_{n+1}^L signify their corresponding determinants. Then

$$\mathrm{d}_{n+1}^L = b\mathrm{d}_n^L - ac\mathrm{d}_{n-1}^L.$$

Proof. This result can be obtained by expanding Q_{n+1}^L in cofactors of the last row or column. ∎

With this result at hand, we can now establish the following Lemma.

LEMMA A.2. *The matrices A_n^L and M_n^L have the same characteristic polynomial.*

Proof. For both matrices, or rather $\mathrm{M}_n^L - \lambda\mathrm{I}$ and $\mathrm{A}_n^L - \lambda\mathrm{I}$ where I is the identity matrix, one obtains the characteristic polynomials as

$$\mathrm{p}_0^L(\lambda) = \lambda^4 + \frac{2+\gamma_L^{(1)}}{1+\gamma_L^{(1)}} c^{(1)^2}\lambda^2,$$

$$\mathrm{p}_1^L(\lambda) = \lambda^5 + \frac{3+2\gamma_L^{(1)}}{1+\gamma_L^{(1)}} c^{(1)^2}\lambda^3 + \frac{1}{1+\gamma_L^{(1)}} c^{(1)^4}\lambda$$

and

$$\mathrm{p}_2^L(\lambda) = \lambda^6 + \frac{4+3\gamma_L^{(1)}}{1+\gamma_L^{(1)}} c^{(1)^2}\lambda^4 + \frac{3+\gamma_L^{(1)}}{1+\gamma_L^{(1)}} c^{(1)^4}\lambda^2.$$

Thus, by recursively applying Lemma A.1, it is clear that all the characteristic polynomials are identical. ∎

An equivalent results is stated as follows.

LEMMA A.3. *The matrices A_n^R and M_n^R have the same characteristic polynomial.*

Proof. For both matrices one obtains the first few characteristic polynomials as

$$\mathrm{p}_0^R(\lambda) = \left[\frac{2}{1+2\gamma_R^{(2)}} + \lambda^2\right]\left(c^{(2)}\right)^2,$$

$$\mathrm{p}_1^R(\lambda) = \left[\left(1 + \frac{2}{1+2\gamma_R^{(2)}}\right)\lambda + \lambda^3\right]\left(c^{(2)}\right)^3,$$

and

$$\mathrm{p}_2^R(\lambda) = \left[\frac{2}{1+2\gamma_R^{(2)}} + \left(2 + \frac{2}{1+2\gamma_R^{(2)}}\right)\lambda^2 + \lambda^4\right]\left(c^{(2)}\right)^4.$$

Hence, from Lemma A.1 it is clear that all the characteristic polynomials are identical. ∎

Finally we have the following Lemma.

LEMMA A.4. *The matrices $A_{m,n}^M$ and $M_{m,n}^M$ have the same characteristic polynomial.*

Proof. It can be verified that the characteristic polynomials, $\mathrm{p}^M_{0,0}$, $\mathrm{p}^M_{1,0}$, $\mathrm{p}^M_{0,1}$, and $\mathrm{p}^M_{1,1}$ are the same for both matrices. Thus, by recursively applying Lemma 0.1, we recover that $\mathrm{p}^M_{m,n} = \mathrm{p}^A_{m,n}$ for all values of m and n. ∎

To finalize the proof of M and A having the same eigenvalues, we need also consider the connection between the various submatrices. For this, we shall need the following result.

LEMMA A.5. *Let Q^L_{n-1}, Q^L_n, and Q^L_{n+1} be the matrices defined in Lemma A.1. Let also Q^R_{m-1} and Q^R_m be matrices defined in a similar way although the block B_k is at the lower right corner. Assume that the matrix S_{m+n+1} is defined as*

$$S_{m+n+1} = \begin{bmatrix} Q^L_n & & & & \\ & & c & & \\ & a & b & c & \\ & & a & & \\ & & & & Q^R_m \end{bmatrix}.$$

Then

$$\mathrm{d}_{m+n+1} = \det[S_{m+n+1}] = b\mathrm{d}^L_n\mathrm{d}^R_m - ac\big(\mathrm{d}^L_n\mathrm{d}^R_{m-1} + \mathrm{d}^L_{n-1}\mathrm{d}^R_m\big).$$

Proof. This result can be obtained by expanding Q_{n+1} in cofactors of $(n+1)$th row (or column). ∎

With this, we now have the tools to state the following.

THEOREM A.1. *The matrices A, Eq.* (27) *with entries given in Eqs.* (A.4)–(A.6), *and M, Eq.* (25), *with entries Eqs.* (A.1)–(A.3), *have the same characteristic polynomial.*

Proof. The statement has been established for the submatrices in Lemma A.2, Lemma A.3, and Lemma A.4. The validity of the statement for the full matrices follows from connecting the submatrices using Lemma A.5. ∎

To prove bounded error behavior, however, we shall also need to establish that the H-norm, using $\mathrm{H} = \mathrm{Q}^T\mathrm{Q}$, is equivalent to the usual discrete L^2-norm, $||\cdot||_h$.

The matrix Q is found by construction under the assumption that it takes the general form illustrated in Eq. (28). In particular,

$$\mathrm{Q}^L = \begin{bmatrix} c^{(1)} & 0 & -\frac{c^{(1)}\gamma^{(1)}_L}{1+\gamma^{(1)}_L} & 0 & & & \\ 0 & \sqrt{1+\gamma^{(1)}_L}\,c^{(1)} & -\frac{q^{(1)}}{\sqrt{1+\gamma^{(1)}_L}} & & 0 & & \\ 0 & q^{(1)} & c^{(1)} & -q^{(1)} & & & \\ 0 & 0 & q^{(1)} & c^{(1)} & -q^{(1)} & & \\ & & & \ddots & \ddots & \ddots & \\ & & & & q^{(1)} & c^{(1)} & -q^{(1)} \\ & & & & & q^{(1)} & c^{(1)} \end{bmatrix},$$

$$Q^M = \begin{bmatrix}
c^{(1)} & -q^{(1)} & & & & & & & & & \\
q^{(1)} & c^{(1)} & -q^{(1)} & & & & & & & & \\
 & \ddots & \ddots & \ddots & & & & & & & \\
 & & q^{(1)} & c^{(1)} & -q^{(1)} & 0 & 0 & 0 & 0 & & \\
 & & & q^{(1)} & c^{(1)} & -q^{(1)} & 0 & 0 & 0 & & \\
 & & & 0 & q_1 & q_2 & q_3 & q_4 & 0 & & \\
 & & & 0 & q_5 & q_6 & q_7 & q_8 & 0 & & \\
 & & & 0 & 0 & 0 & q^{(2)} & -c^{(2)} & -q^{(2)} & & \\
 & & & 0 & 0 & 0 & 0 & q^{(2)} & -c^{(2)} & -q^{(2)} & \\
 & & & & & & & \ddots & \ddots & \ddots & \\
 & & & & & & & & q^{(2)} & -c^{(2)} & -q^{(2)} \\
 & & & & & & & & & q^{(2)} & -c^{(2)}
\end{bmatrix},$$

and

$$\mathrm{Q}^R = \begin{bmatrix}
-c^{(2)} & -q^{(2)} & & & \\
q^{(2)} & -c^{(2)} & -q^{(2)} & & \\
 & \ddots & \ddots & \ddots & \\
 & & q^{(2)} & -c^{(2)} & -q^{(2)} \\
 & & 0 & \sqrt{\frac{2}{1+2\gamma_R^{(2)}}}q^{(2)} & -\sqrt{\frac{1+2\gamma_R^{(2)}}{2}}c^{(2)}
\end{bmatrix}.$$

Here we have, for simplicity, introduced the new variables

$$q^{(1)} = -\frac{c^{(1)}}{2}\sqrt{2\gamma_R^{(1)^2} + 4\gamma_R^{(1)^2}}, \quad q^{(2)} = \frac{c^{(2)}}{2}\sqrt{2 - 6\gamma_R^{(1)} + 4\gamma_R^{(1)^2}},$$

$$q_1 = \frac{c^{(1)}}{2}\sqrt{2\gamma_R^{(1)} + 4\gamma_R^{(1)^2}}, \quad q_2 = -\frac{c^{(1)}}{2}\big(1 + 2\gamma_R^{(1)}\big),$$

$$q_3 = -\frac{c^{(2)}}{2}\sqrt{2 - 6\gamma_R^{(1)} + 4\gamma_R^{(1)^2}}, \quad q_4 = -\frac{c^{(2)}}{2}\big(1 - 2\gamma_R^{(1)}\big),$$

$$q_5 = -\frac{c^{(1)}}{2}\sqrt{2\gamma_R^{(1)} - 4\gamma_R^{(1)^2}}, \quad q_6 = \frac{c^{(1)}}{2}\sqrt{1 - 4\gamma_R^{(1)^2}},$$

$$q_7 = -\frac{c^{(2)}}{2}\sqrt{2 + 2\gamma_R^{(1)} - 4\gamma_R^{(1)^2}}, \quad q_8 = -\frac{c^{(2)}}{2}\sqrt{1 - 4\gamma_R^{(1)^2}}.$$

It is only left to prove that $||\cdot||_H$ is L^2-equivalent. This, however, follows from the inequalities

$$\begin{aligned}
k_1^2 &= \frac{\min\left\{c^{(1)^2}, c^{(1)^2}\right\}}{4} \\
&\leq \frac{1}{4}\big(\mathbf{u},\ \mathrm{diag}\big(c^{(1)^2}, \ldots, c^{(1)^2}, c^{(2)^2}, \ldots, c^{(2)^2}\big)\mathbf{u}\big)_h \\
&\leq (\mathbf{u},\ Q^T Q\mathbf{u})_h
\end{aligned}$$

$$\leq 4\big(\mathbf{u},\ \mathrm{diag}\big(c^{(1)^2},\ldots,c^{(1)^2},c^{(2)^2},\ldots,c^{(2)^2}\big)\mathbf{u}\big)_h$$
$$\leq 4\max\left\{c^{(1)^2},c^{(1)^2}\right\}=k_2^2;\quad \|\mathbf{u}\|_k=1.$$

The lower bound is found by using the fact that Q^TQ is a diagonally dominant matrix and it stays diagonally dominant even after subtracting a diagonal matrix of the form $\frac{1}{4}\mathrm{diag}(c^{(1)^2},\ldots,c^{(1)^2},c^{(2)^2},\ldots,c^{(2)^2})$. The upper bound is derived by bounding all the terms in $(\mathbf{u},Q^TQ\mathbf{u})_h$, taking the form $2\alpha_{i,j}u_iu_j$ by $|\alpha_{i,j}|(u_i^2+u_j^2)$. Thus $k_1\leq\|Q\|_h\leq k_2$. Moreover, since Q^TQ is a (strictly) positive definite matrix, Q must be a nonsingular matrix, and $\|Q^{-1}\|_h$ can be bounded as $1/k_2\leq\|Q^{-1}\|_h\leq 1/k_1$.

ACKNOWLEDGMENT

This work was partially supported by AFOSR Grant F49620-96-1-0426, NSF Grant DMS-0074257, and DOE Grant 98-ER-25346. JSH acknowledges partial support as a Sloan Research Fellow from the Alfred P. Sloan Foundation.

REFERENCES

1. A. Taflove (Ed.), *Advances in Computational Electrodynamics: The Finite-Difference Time-Domain Method* (Aztech House, Boston, 1998).
2. B. Yang, D. Gottlieb, and J. S. Hesthaven, Spectral simulations of electromagnetic wave scattering, *J. Comput. Phys.* **134**, 216 (1997).
3. B. Yang and J. S. Hesthaven, A pseudospectral method for time-domain computation of electromagnetic scattering by bodies of revolution, *IEEE Trans. Antennas Propagation* **47**, 132 (1999).
4. J. S. Hesthaven, P. G. Dineser, and J. P. Lynov, Spectral collocation time-domain modeling of diffractive optical elements, *J. Comput. Phys.* **155**, 1 (1999).
5. K. S. Yee, Numerical solution of initial boundary value problems involving Maxwell's equations in isotropic media, *IEEE Trans. Antennas Propagation* **14**, 302 (1996).
6. B. Yang and D. Gottlieb, Comparisons of staggered and non-staggered schemes for Maxwell's equations in *Proceedings of the 12th Annual Review of Progress in Applied Computational Electromagnetics*, (Naval Postgraduate School, Monterey, CA, March 1996) Vol. II, pp. 1122–1131.
7. A. Taflove, *Computational Electrodynamics—The Finite-Difference Time-Domain Method* (Aztech House, Boston, 1995).
8. A. C. Cangellaris and D. B. Wright, Analysis of the numerical error caused by the stairstepped approximation of a conducting boundary in FDTD simulations of electromagnetic phenomena, *IEEE Trans. Antennas Propagation* **39**, 1518 (1991).
9. R. Holland, Pitfalls of staircase meshing, *IEEE Trans. Electromag. Compatibility* **35**, 434 (1993).
10. A. Akyurtlu, D. H. Werner, V. Veremey, D. J. Steich, and K. Aydin, Staircasing errors in FDTD at an air-dielectric interface, *IEEE Trans. Microwave Guided Wave Lett.* **9**, 444 (1999).
11. P. Monk and E. Suli, Error estimates of Yee's method on non-uniform grids, *IEEE Trans. Magnetics* **30**, 393 (1994).
12. K. S. Yee, J. S. Chen, and A. H. Chang, Conformal finite-difference time-domain (FDTD) with overlapping grids, *IEEE Trans. Antennas Propagation* **40**, 1068 (1992).
13. Y. Hao, and C. J. Railton, Analyzing electromagnetic structures with curved boundaries on Cartesian FDTD meshes, *IEEE Trans. Antennas Propagation* **46**, 82 (1998).
14. T. G. Jurgens, A. Taflove, K. Umashaankar, and T. G. Moore, Finite-difference time-domain modeling of curved surfaces, *IEEE Trans. Antennas Propagation* **40**, 357 (1992).
15. R. Holland, Finite difference solutions of Maxwell's equations in generalized nonorthogonal coordinates, *IEEE Trans. Nuclear Sci.* **30**, 4589 (1983).

16. M. Fusco, FDTD algorithm in curvilinear coordinates, *IEEE Trans. Antennas Propagation* **38**, 76 (1990).
17. A. H. Mohammadian, V. Shankar, and W. F. Hall, Computation of electromagnetic scattering and radiation using a time-domain finite-volume discretization procedure, *Comput. Phys. Comm.* **68**, 175 (1991).
18. K. S. Yee and J. S. Chen, The finite-difference time-domain (FVTD) and the finite-volume time-domain (FVTD) methods in solving Maxwell's equations, *IEEE Trans. Antennas Propagation* **45**, 354 (1997).
19. E. Luo and H. O. Kreiss, Pseudospectral vs. finite difference methods for initial value problems with discontinuous coefficients, *SIAM J. Sci. Comput.* **20**, 148 (1999).
20. C. Zhang and R. J. LeVeque, The immersed interface method for acoustic wave equations with discontinuous coefficients, *Wave Motion* **25**, 237 (1997).
21. B. Gustafsson, The convergence rate for difference approximations to mixed initial boundary value problems, *Math. Comp.* **29**, 396 (1975).
22. B. Gustafsson, H. O. Kreiss, and J. Oliger, *Time Dependent Problems and Difference Methods* (Wiley, New York, 1995).
23. A. Ditkowski, *Bounded-Error Finite Difference Schemes for Initial Boundary Value Problems on Complex Domains*. Ph.D. thesis (Department of Applied Mathematics, School of Mathematical Sciences, Tel-Aviv University, Tel-Aviv, Israel, 1997).
24. S. Abarbanel, A. Ditkowski, and A. Yefet, Bounded-error schemes for the wave equation on complex domains, submitted for publication.
25. A. Yefet and P. G. Petropoulos, A non-dissipative staggered fourth-order accurate explicit finite difference scheme for the time-domain Maxwell's equations, ICASE Report 99-30 (NASA Langley Research Center, VA, 1999).